Gad1-promotor-driven GFP expression in non-GABAergic neurons of the nucleus endopiriformis in a transgenic mouse line

Sophie Riedemann[1], Bernd Sutor[1], Matteo Bergami[2, 3] and Therese Riedemann[1*]

[1]Ludwig-Maximilians-University, Biomedical Center, Physiological Genomics, Großhaderner Strasse 9, 82152 Munich, Germany

[2]Cologne Excellence Cluster on Cellular Stress Responses in Aging-Associated Diseases (CECAD) and University Hospital of Cologne, Joseph-Stelzmann-Straße 26, D-50931, Cologne, Germany.

[3]Center for Molecular Medicine (CMMC), University of Cologne, Robert-Koch-Str. 21, D-50931, Cologne, Germany.

[*]Corresponding author

E-Mail: therese.riedemann@med.uni-muenchen.de

Acknowledgements

We are grateful to Gabi Horn for excellent technical assistance. T.R. is supported by the Friedrich-Baur Stiftung (grant number 03/16). M.B. is supported by the European Research Council (ERC-StG-2015, grant number 67844).

Abstract

Transgenic animals have become a widely used model to identify and study specific cell types in whole organs. Promotor-driven reporter gene labeling of the cells under investigation has promoted experimental efficacy to a large degree. However, rigorous assessment of transgene expression specificity in these animal models is highly recommended in order to validate cellular identity and to isolate potentially mislabeled cell populations. Here, we report

on one such mislabeled neuron population in a widely used transgenic mouse line in which GABAergic somatostatin-expressing interneurons (SOM^{pos} INs) are labeled by eGFP (so-called GIN mouse, FVB-Tg(GadGFP)45704Swn/J). These neurons represent a subpopulation of all SOM^{pos} INs. However, we report here on GFP labeling of non-GABAergic neurons in the nucleus endopiriformis of this mouse line.

Keywords: GABA, interneurons, eGFP, GAD67-promotor, off-target labeling, nucleus endopiriformis

Introduction

Transgenic animals expressing reporter genes such as the enhanced green fluorescent protein (eGFP) under the control of specific promotors have become widely used experimental models when studying the properties of certain cell types. Their use is of particular advantage when the cell types under investigation are rare, display diverse properties and when the probability of finding them in a wild-type animal is low. Since they facilitate cell identification, in particular during acute electrophysiological experiments, transgenic animals with specific promotor-driven expression of reporter genes helped to reduce the number of animals necessary to perform scientific projects. However, the cellular phenotypes of a common genotype can be considerably diverse (see e.g. Riedemann, Schmitz & Sutor et al., 2016a; Riedemann, Straub & Sutor 2018) and it is therefore advisable to characterize the properties of cells that are genetically labeled with reporter genes. This is especially important in research fields where the aim is to classify cells according to their molecular, biochemical, morphological or physiological properties. The classification of GABAergic interneurons in the cerebral cortex is based on the very same properties listed above. Based on those properties, it is strived to allocate interneurons to specific classes or subclasses (Ascoli et al., 2008; DeFelipe et al., 2013). In many studies, this characterization is performed on cells genetically labeled with eGFP and it is comprehensible that such

studies have to rely on unambiguously identified cells. However, genetic labeling with fluorescent reporter genes might lead to a false sense of security if the labeling targets not only the cell type under investigation. Hu, Cavendish and Agmon (2013) reported on off-target labeling in the somatostatin (SST)-Cre mouse resulting in a false positive labeling of 6-10% of parvalbumin-expressing (PV^{pos}) interneurons. Another transgenic mouse line commonly used to study SOM^{pos} interneurons is the so-called GIN (green fluorescent protein-expressing interneurons) mouse (FVB-Tg(GadGFP)45704Swn/J). Here, the reporter gene labels a subpopulation of SOM^{pos} interneurons (Halabisky, Shen, Huguenard & Prince, 2006; Kinnischtzke, Sewall, Berkepile & Fanselow, 2012; Ma, Hu, Berrebi, Mathers & Agmon, 2006; McGarry et al., 2010; Oliva, Jiang, Lam, Smith & Swann, 2000; Riedemann et al., 2016a, 2018; Xu, Roby & Callaway, 2006, 2010;). SOM^{pos} interneurons represent a very diverse group of cells with various neurochemical phenotypes and morphologies. Despite the fact that also their electrophysiological properties differ greatly, it is possible to distinguish them clearly from pyramidal neurons or from PV^{pos} interneurons (Kawaguchi & Kubota, 1996; Riedemann et al., 2018). In the study presented here, we report on GFP labeling deep to the cortical projection neurons of the GIN mouse leading to the delineation of the dorsal nucleus endopiriformis (Majak & Moryś, 2007; Mathur, 2014; Smith et al., 2018; Watson, Smith & Alloway, 2017). We refer to these GFP^{pos} neurons in the nucleus endopiriformis as endopiriform population (EPP) in order to distinguish them from SOM^{pos} GIN in other brain areas. The GFP^{pos} EPP neurons do not express somatostatin and, more surprisingly, they are not GABAergic. Our investigations suggest that these neurons developed a glutamatergic phenotype.

Materials and Methods

Animals

All experiments were approved by the institutional committees on animal care (Core Facility Animal Models / Ludwig-Maximilians-University Munich) and by the Bavarian State

authorities, conforming to international guidelines on the ethical use of animals. Experiments were performed on animals of the transgenic mouse line FVB-Tg(GadGFP)45704Swn/J (Oliva et al., 2000), where in a subset of GABAergic interneurons the enhanced green fluorescent protein (eGFP) is expressed under the control of the glutamic acid decarboxylase 67 (GAD67) promotor. Animals were obtained from Jackson Laboratories (ME, USA) and were bred in the institute's animal facility. The age of the mice used ranged between 1 and 68 days.

Acute slice preparation

Preparation of coronal slices (thickness: 300 µm) was performed as previously described (Riedemann et al., 2016b, 2018). The cutting solution consisted of (in mM): N-methyl-D-glucamine (135), KCl (1.5), KH_2PO_4 (1.5), $NaHCO_3$ (23), $CaCl_2$ (0.5), $MgCl_2$ (3.5), ascorbic acid (0.4) and D-glucose (25), (pH at 28°C: 7.4, osmolarity: 310 – 330 mOsm). Prior to decapitation, the animals were deeply anaesthetized by exposure to CO_2 until the extinction of all reflexes. After the cutting procedure, the slices were collected and submerged in artificial cerebro-spinal fluid (ASCF) containing (in mM): NaCl (125), KCl (3), NaH_2PO_4 (1.25), $NaHCO_3$ (25), $CaCl_2$ (2), $MgCl_2$ (2), ascorbic acid (0.4) and D-Glucose (25). All solutions were continuously perfused with 95% O_2 / 5% CO_2 in order to maintain a pH of 7.4. The slices were incubated for 30 min at 28°C and for another 90 min at room temperature. For electrophysiological analysis, single slices were transferred to a recording chamber mounted on the stage of an upright microscope (Zeiss Axioskop FS equipped with a 40x objective, 0.75 numerical aperture [NA]). Electrophysiological recordings were performed at a bath temperature of 27-28°C.

Whole-cell recordings

All GFP-expressing neurons were visualized and identified by means of an upright microscope equipped with differential-interference-contrast (DIC)-infrared optics and epifluorescence (filter set: Zeiss BP450-490, LP520). Pyramidal neurons were identified by the triangular shapes of their somata and their relatively thick apical dendrites. Fluorescence

and infrared images were acquired with the help of a CCD camera (Orca-ER, Hamamatsu, Shizouka, Japan). The recording electrodes were fabricated from borosilicate glass capillaries (OD: 1.5 mm, ID: 0.86 mm, Hugo Sachs Elektronik-Harvard Apparatus, March-Hugstetten, Germany) and were filled with a solution containing (in mM): K-gluconate (135), KCl (4), NaCl (2), EGTA (0.2), HEPES (10), Mg-ATP (4), Na-GTP (0.5), and phosphocreatine (10) (osmolarity 290, pH 7.3). Biocytin (0.3 – 0.5%) was added to the electrode solution. The electrodes had resistances ranging between 4 and 8 MΩ and were connected to the amplifier's headstage via a chlorided silver wire. A silver / silver chloride – pellet immersed into the recording solution served as reference electrode. Somatic whole-cell recordings were made in the current-clamp and in the voltage-clamp mode using an ELC 03XS amplifier (npi electronics, Tamm, Germany). Bias and offset current were zeroed before giga seal formation. After rupture of the membrane, the electrode capacitance and series resistance were compensated as described by Riedemann, Polder and Sutor (2016b).

Analysis of electrophysiological parameters

Passive membrane properties (input resistance, membrane time constants, cell input capacitance) were analyzed as previously described by Riedemann et al. (2018). Analysis of the current-voltage relationships (IV-curves) was performed by injection of hyper- and depolarizing current steps (1000 ms in duration) into the cells. The step amplitudes and the step increments (5-20 pA) were adjusted to cover a membrane potential range between about -100 mV and just subthreshold levels. The current-voltage relationship was analyzed in the initial phase (usually around 70 - 150 ms post current step onset when the hyperpolarizing voltage response was maximal) and in the steady state (i.e. at the end of the current pulses). The voltage responses were then plotted as a function of the current intensities and the corresponding data points were interpolated using the smoothing spline algorithm supplied by IGOR Pro 6 (WaveMetrics, Lake Oswego, USA). Differentiation of the interpolated IV-curve yielded the slope resistance as a function of the current injected (so-called R_N-curve). The rectifying properties of the current-voltage relationship were compared by normalizing the R_N-curve to the steady state slope resistance at resting membrane

potential (i.e. input resistance at 0 pA derived from the R_N-curve). The rectification index (i.e. the relation of the input resistances at any potential to that at resting membrane potential) was determined at a membrane potential of about -100 mV.

The properties of single action potentials were derived from recordings in which action potentials were elicited by means of just suprathreshold current steps or ramps (50 ms in duration). The spikes were analyzed as described by Riedemann et al. (2018). For the analysis of action potential discharge patterns, 30 depolarizing current steps (1000 ms in duration) with increments of usually 5-20 pA were injected. To investigate the properties of the discharge patterns quantitatively, we determined the firing frequencies from the interspike intervals (ISI) and plotted these values as a function of the spike times. These *F-t*-relationships were determined for all effective current strengths yielding an array of curves from which the following parameters were derived: (1) ratio of the frequencies of the first and the second ISI (F_{ISI1} and F_{ISI2}), (2) ratio of the frequencies of the first and the last ISI ($F_{ISILast}$) (i.e. adaptation index), (3) ratio of the frequency of the first ISI to the mean frequency ($F_{ISIMean}$). All these measurements were performed at current strengths, where we did neither encounter fluctuation driven discharge (Schreiber, Samengo & Herz, 2009) nor action potential shunting.

In order to detect spontaneous synaptic activity, we performed voltage-clamp recordings for 3 to 5 minutes at holding potentials of -60 mV or -70 mV. Spontaneous postsynaptic currents (PSCs) were automatically detected using the algorithm provided by the NeuroMatic plugin (version 2.00) for IgorPro 6. The detection threshold was set to 10 pA. Only monophasic synaptic currents were analyzed and the following parameters were determined: PSC frequency, peak amplitude and duration at half-maximal amplitude.

Data acquisition and analysis

Recorded voltage signals were amplified (x 20), filtered at 20 kHz and digitized at sampling rates of 10 or 20 kHz. Current signals were recorded at a gain of 1 V/nA, filtered at 3 kHz and digitized at sampling rates of 10 or 20 kHz. Data acquisition and generation of command pulses was accomplished by means of an analogue-digital converter (Power3, Cambridge

Electronic Design, UK) in conjunction with the Signal data acquisition software (Version 6, Cambridge Electronic Design, UK). Data analysis was performed using IGOR Pro 6 (WaveMetrics, Lake Oswego, USA) together with the NeuroMatic IGOR plugin (version 2.00, www.neuromatic.thinkrandom.com).

Visualization of biocytin-injected neurons

At the end of the recordings, the biocytin-filled patch-pipettes were very carefully withdrawn from the somata of the neurons. The slices were fixed for 12 hours in phosphate-buffered saline (PBS) containing freshly prepared 4% paraformaldehyde. After fixation, slices were washed with PBS containing 0.3% Triton-X100 and kept in this solution for 48 hours. Neurons were visualized by incubating the slices in Alexa 594- or Alexa 488-coupled streptavidine (diluted 1:1000 in PBS, Molecular Probes, USA) for at least 48 hours.

Tissue preparation for immunocytochemistry

Animals were deeply anaesthetized and transcardially perfused with warm (37°C) PBS followed by ice-cold 4% paraformaldehyde (PFA). Isolated brains were postfixed in 4% PFA overnight. Then, the brains were transferred successively to 10%, 20% and 30% sucrose solutions (in phosphate-buffered saline, PBS) until the brains sank. Free-floating sections (thickness: 30 to 50 µm) were cut on a cryostat (CM3050, Leica, Wetzlar, Germany) and transferred to clean 24-well plates. The sections were washed twice with PBS and stored in PBS containing 0.3% Triton-X100 (PBS-T) until further use.

Retrograde labeling of frontal cortex projection neurons

Isolated brains were fixed in 4% PFA overnight. A 1,1'-dioctadecyl-3,3,3'3'-tetramethylindocarbocyanine perchlorate (DiI) crystal (Molecular probes, Waltham, MA, USA, D3911) was placed in the left anterior cingulate cortex (see Fig. S2) and the brains were kept in 4% PFA for five days and then transferred to PBS. Four weeks after DiI application, the brains were cryopreserved in 30% sucrose. Coronal brain sections of 50 µm thickness were cut on a cryostat (CM3050). Immediately after the cutting procedure, cell nuclei were

visualized by DAPI staining and the sections were mounted with a MOWIOL-based mounting medium (Marx, Gunter, Hucko, Radnikow & Feldmeyer, 2012).

Labeling for immunofluorescence

The analysis of the endopiriform population of GFP^{pos} neurons was performed on serial coronal sections of the corresponding brain regions (Fig. 1a). To this end, every sixth section roughly between bregma 2.00 and -2.00 (according to Franklin & Paxinos, 2012) was collected and analyzed. The neurochemical profiles of all cells were determined by incubating the sections with different combinations of primary antibodies. Prior to antibody incubation, sections were blocked in PBS-T containing 5% normal goat serum (NGS) and 2.5% bovine serum albumin (BSA) for at least 2 hours.

The following primary antibodies were used: chicken anti-GFP (Millipore, Billerica, MA,USA, 06-896, dilution: 1:400, RRID: AB_310288), rabbit anti-GAD65/67 (1:2000; Sigma-Aldrich, St. Louis, MO,USA, G5163, polyclonal, RRID: AB_477019), mouse anti-NeuN (1:200, Millipore, Billerica, MA,USA, MAB377, monoclonal, RRID: AB_2057032), rat anti-somatostatin (1:200, Millipore, MAB354, monoclonal, RRID: AB_2255365), mouse anti-parvalbumin (1:1000, SWANT, 235, monoclonal, RRID: AB_10000343) and mouse anti-αCaMKII (1:400; Sigma-Aldrich, C6974, polyclonal, RRID: AB_258984). All primary antibodies were diluted in PBS-T containing 3% NGS and the slices were incubated in the presence of the antibodies for 24 – 48 hours on a horizontal shaker at 4°C. The primary antibodies used in this study were tested for optimal dilution (usual titration range: 1:100, 1:200, 1:400, 1:800, 1:2000; 1:5000, 1:10000).

The secondary antibody directed against chicken was Alexa Fluor 488-conjugated goat anti-chicken IgG (Invitrogen, Waltham, MA, USA, A11039, 1:500; RRID: AB_10563770). Secondary antibodies directed against mouse were: Alexa Fluor 594-conjugated goat anti-mouse IgG (Molecular Probes, Waltham, MA, USA, A-11032, 1:500; RRID: AB_10562708), Cy3-conjugated goat anti-mouse IgG (Dianova, Hamburg, Germany, 115-165-003, 1:500, RRID: AB_2338680), Dylight 649-conjugated goat anti-mouse IgG (Dianova, 115-606-072, 1:500; RRID: AB_2338928). Secondary antibodies against rabbit were as follows: Cy3-

conjugated donkey anti-rabbit (Dianova, 711-165-152, 1:500; RRID: AB_2307443), Cy5-conjugated goat anti-rabbit IgG (Dianova, 111-175-144; 1:500; RIID: AB_2338013), Alexa Fluor 647-conjugated goat anti-rabbit IgG (Dianova, 111-605-144, 1:500; RRID: AB_2338078). Secondary antibodies against rat included: Cy3-conjugated goat anti-rat IgG (Dianova, 112-165-167, 1:500; RRID: AB_2338251), Alexa Fluor A647-conjugated goat anti-rat (Molecular Probes, A-21247, 1:500; RRID: AB_10563568), and Dylight 649-conjugated goat anti-rat IgG (Rockland, 612-143-002, 1:1000; RRID: AB_11180061). Following secondary antibody incubation, slices were washed extensively before being wet-mounted onto a glass-slide with a MOWIOL-based mounting medium (Marx et al., 2012).

Antibody specificity

Each primary antibody was tested individually before being used in different combinations with other antibodies as described previously by Riedemann et al. (2016a). According to the data sheets provided by the suppliers, all of the antibodies were tested for specificity and displayed no detectable cross-reactivity with any other proteins and peptides which were used in our experiments. In addition, each secondary antibody used in the present study was tested for non-specific binding alone or in combination with other secondary antibodies. Moreover, primary antibodies were visualized with different secondary antibodies and only those secondary antibodies were used that produced the same labeling pattern.

Imaging

Immunostainings were analyzed with a LSM710 laser scanning microscope (Zeiss) or with a Axio Observer Z1 epifluorescence microscope (Zeiss). Digital images were captured using the ZEN software (Zeiss). DAPI was excited at 405 nm (diode laser), GFP was visualized at 488 nm (argon laser), Alexa 594/Cy3-conjugated probes at 561 nm (Helium/Neon, He/Ne laser), and Alexa 647-/Dylight649-conjugated probes at 633 nm (He/Ne laser). The fluorescent signals were detected in a sequential mode and all fluorescence emission filters were non-overlapping. Z-stacks through the depth of the sections (30-50 µm) were acquired and the individual images collapsed onto one focal plane (maximum intensity projection). Z-

stack intervals ranged from 1.0 - 2.5 µm depending on the objectives used. Images were scanned using the following objectives: 10× air (NA = 0.3), 25× water (NA = 0.8), and 40× water (NA = 1.1). Images were scanned at the following resolutions: 1024 x 1024, 2048 x 2048 or 4096 x 4096 pixels.

Image Analysis

Using the ZEN software (2011, Zeiss, Jena, Germany), all images were converted into TIFF files and image analysis was performed using ImageJ (National Institute of Health, USA). With the help of a counting frame to allow for a standardized quantification, all cells within in a given image were counted manually. All cells that remained visible after background subtraction were considered to express a given antigen. The counting frame was divided into three so-called sectors (Fig. 1c and d) and was placed on top of all images acquired with the 10×air objective. These counts were related to the total number of GFP^{pos} neurons in the counting frame.

For colocalization analysis, images were acquired using the 40× water objective. Two images of GFP^{pos} neurons within the nucleus endopiriformis were taken per hemisphere and both hemispheres were analyzed. The sum of all GFP^{pos} neurons from all animals analyzed was determined and coexpression of any neurochemical marker is given as a fraction of the total GFP^{pos} cell number in one complete set of experiments.

Morphological reconstruction and morphometric analysis of biocytin-injected neurons

Neurons labeled with biocytin were reconstructed manually using the Neurolucida software (Micro Bright Field, USA). Confocal image stacks of biocytin-filled neurons were uploaded into the software and the correct voxel dimensions were adjusted. Dendrites and axons (partial reconstruction of axons) were traced individually. Measurements of dendritic and axonal length, of dendritic and axonal nodes, dendritic complexity and Sholl analyses were performed with the help of the Neurolucida Explorer software. In addition, polar histograms of the dendritic trees were obtained by generating a round histogram where length was plotted

as a function of direction (from 0 to 360°), each bin was then normalized to the total dendritic length and a vector was calculated as the sum of all bins and their corresponding orientation. The dendritic complexity was calculated from: [Sum of the terminal orders + Number of terminals] * [Total dendritic length / Number of primary dendrites]. Sholl analysis of dendritic and axonal processes was performed by spacing Sholl discs in 20 µm intervals. The following variables were included into the morphometric analysis: total length of the dendritic tree, total length of the axonal tree, total number of dendritic branching points, total number of axonal branching points, number of primary dendrites, direction of axon and origin of axon.

Statistics

The distribution of GFP^{pos} cells within the nucleus endopiriformis as well as their neurochemical profile was evaluated in four animals. The morphometric analysis was performed on 10 GFP^{pos} cells and 4 GFP^{neg} cells of the nucleus endopiriformis and, in addition, on 5 GIN and 5 layers II and III pyramidal neurons of the somatosensory cortex. Electrophysiological data were obtained from 45 GFP^{pos} and 29 GFP^{neg} cells of the nucleus endopiriformis and 24 GIN and 12 layer II and III pyramidal neurons of the somatosensory cortex.

All electrophysiological and morphometric data obtained from the respective cell groups were compared to detect significant differences between groups. First, the distribution pattern of the data (normal or non-normal) was tested using the D'Agostino and Pearson Omnibus Normality test. In case of a normal distribution of data points, one-way analysis of variance (One-way ANOVA) was performed with Bonferroni post tests. In case of a non-normal distribution of data points, Kruskal-Wallis test with Dunn's post test was performed. Significance levels were $p<0.05$, $p<0.01$ and $p<0.001$.

All data are expressed as means ± standard deviation (SD) unless indicated otherwise. Data analysis and statistics were performed in Excel (Microsoft, USA), in GraphPad Prism (LaJolla, USA) or in IGOR Pro (Version 6, Wavemetrics, USA).

Results

GFP^{pos} cells are located in the endopiriform nucleus

Qualitative analysis of the localization of GFP^{pos} EPP neurons revealed that the majority of these neurons were located within the nucleus endopiriformis (Fig. 1a and supplemental Fig. 1). This finding was supported by analysis of the expression of the calcium-binding protein parvalbumin (PV) in the claustrum and nucleus endopiriformis and by analysis of retrograde DiI labeling of cingulate cortex projection neurons. In agreement with previous reports on PV expression in the nucleus endopiriformis (Real, Dávila & Guirado, 2003; Wang et al., 2017), we only found scarce immunoreactivity to PV in the region with the highest density of GFP^{pos} neurons (Fig. 1b). Furthermore, previous studies reported on a strong connectivity between the claustrum-endopiriform complex and the anterior cingulate and infralimbic cortex (Behan & Haberly, 1999; Condé, Maire-Lepoivre, Audinat & Crepel, 1995; Qadir et al., 2018; Smith et al., 2018; Wang et al., 2017; Watson et al., 2017; White et al., 2017; Zingg, Dong, Tao & Zhang, 2018). Therefore, we injected a DiI crystal into the anterior cingulate cortex and determined the presence of DiI-positive fibers in the area with the highest density of GFP^{pos} neurons (Fig. S2). As can be seen from Fig. S2, we observed DiI-positive fibers in close proximity to GFP^{pos} neurons corroborating the finding that GFP^{pos} neurons are located within the claustrum-endopiriform complex. In summary, analysis of PV immunoreactivity in the region with the highest density of GFP^{pos} neurons and the observation of DiI-positive fibers in close vicinity to GFP^{pos} neurons suggest that these cells are mostly located within the nucleus endopiriformis.

According to the literature (Halabisky et al., 2006; Ma et al., 2006; Oliva et al., 2000; Riedemann et al., 2016a, 2018; Xu et al., 2006; 2010), the GFP^{pos} EPP neurons should represent somatostatinergic green fluorescent protein expressing interneurons (GIN). Therefore, we analyzed SOM expression in GFP^{pos} EPP neurons and in GIN of the piriform cortex. To this end, a counting grid consisting of three sectors was placed on top of the nucleus endopiriformis and the piriform cortex and the GFP^{pos} cells and SOM^{pos} interneurons

(SOM^{pos} IN) were counted in all three sectors. Altogether, we counted 2524 SOM^{pos} INs in the piriform cortex and endopiriform nucleus of four animals. Surprisingly, colocalization of GFP and SOM in cells of the putative nucleus endopiriformis was virtually absent (0.3% ± 0.1 SEM; Figs. 1d, e, Fig. 2a). However, the GFP^{pos} neurons of the more superficial piriform cortex (corresponding to sectors II and III) showed partial to substantial coexpression of GFP and SOM (Fig. 1e). In detail, we found SOM expression in 11.8% (± 1.4 SEM) of GFP^{pos} cells of sector II and in 80.3% (± 2.6 SEM) of GFP^{pos} cells in sector III (Fig. 1e, left panel). Reversely, we found that only 1.8% (± 0.4 SEM) of all SOM^{pos} INs counted in sector I mostly corresponding to nucleus endopiriforms were GFP^{pos}. In sector II 13.2% (± 3.3 SEM) of all SOM^{pos} INs were also positive for GFP and around 37.3% (± 6.4 SEM) of all SOM^{pos} INs in sector III were GFP^{pos} (Fig. 1e, right panel).

Neurochemical properties of GFP^{pos} cells of the endopiriform nucleus

Given the finding that SOM expression in GFP^{pos} EPP cells was virtually absent (Fig. 1e, Fig. 2a), we next tested PV expression in these cells. In the cerebral cortex, PV is often used as a marker for fast-spiking interneurons and exhibits almost no colocalization with SOM (Nasser et al., 2015; Rudy, Fishell, Lee & Hjerling-Leffler, 2011), but colocalization of SOM^{pos} neurons with PV was reported in the endopiriform region of the rat (Kowiański et al., 2004). As described above, we only found scarce immunoreactivity to PV in the putative nucleus endopiriformis and found no evidence for PV expression in GFP^{pos} EPP cells (0 out of 612 GFP^{pos} cells, n=4 animals, Fig. 2b).

The results presented so far cast doubt on the present assumption that all GFP^{pos} cells of the GIN mouse are GABAergic interneurons. Therefore, coexpression of the GABA-synthetizing enzymes GAD65 and GAD67 with GFP was tested in GFP^{pos} EPP cells. Surprisingly, more than 98% of all GFP^{pos} cells counted (98.6% ± 0.3 SEM; n=3 animals) showed no immunoreactivity to GAD65/67 indicating a non-GABAergic phenotype (Fig. 2c). GAD65/67 expression was found in less than 2% of all GFP^{pos} cells tested (1.5% ± 0.4 SEM). In

contrast, 96.2% (± 1.1 SEM) of SOM^{pos} INs of the piriform cortex showed immunoreactivity to GAD65/67.

Due to the observation that GFP^{pos} EPP cells were non-GABAergic, we next tested whether these cells expressed αCaMKII, a specific marker for glutamatergic projection cells (McDonald, Muller & Mascagni, 2002). We performed triple immunolabelings for GFP, αCaMKII and GAD65/67. Unexpectedly, we found αCaMKII expression in around 91% of all GFP^{pos} EPP cells (91.4% ± 1.1 SEM; Fig. 2d, n=4 animals). At the same time, we could not detect coexpression of αCaMKII and GAD65/67 (0.5% ± 0.04 SEM), indicating that these markers labeled two different neuron populations. Moreover, we found that αCaMKII^{pos} and GAD65/67^{pos} cells are present at a ratio of around 9:1 (4105 αCaMKII^{pos} cells vs. 430 GAD65/67^{pos} cells) within the nucleus endopiriformis (Fig. 2c). Given the fact that the nucleus endopiriformis is discussed to be part of the ventral claustrum (Kowiański, Dziewiatkowski, Kowiańska & Moryś, 1999; Majak, et al., 2000; Majak, Pikkarainen, Kemppainen, Jolkkonen & Pitkänen, 2002; Mathur, 2014; Smith et al., 2018; Watson & Puelles, 2017; Watson et al., 2017) and that the claustrum and nucleus endopiriformis exhibit a similar degree of connectivity (Behan & Haberly, 1999; Majak & Moryś, 2007; Watson et al., 2017), this ratio is in good agreement with previous reports showing that around 6-12% of all claustral neurons are GABAergic interneurons (Braak & Braak, 1982; Gomez-Urquijo, Gutiérrez-Ibarluzea, Bueno-López & Reblet, 2000; Kowiański, Moryś, Dziewiatkowski, Wójcik, Sidor-Kaczmarek & Moryś, 2008). In order to answer the question of whether these GFP^{pos} EPP neurons were born as GABAergic interneurons and only adopted a glutamatergic phenotype later in development, we performed immunolabelings for GFP, GAD65/67, SOM and αCaMKII at postnatal day one (P1). At that age, most GFP^{pos} EPP cells neither expressed GAD65/67 nor SOM (Fig. S3). However, αCaMKII expression could already be observed in some albeit not all GFP^{pos} cells (Fig. S3).

Given their high local density in the nucleus endopiriforms and given the fact that GFP^{pos} EPP neurons were neurochemically distinct from cortical GIN, we wanted to rule out that these cells were remnants of migrating neurons or dying cells. Therefore, we compared the

properties of GFP^{pos} EPP neurons in all following experiments not only to cortical GIN and pyramidal neurons but also to GFP^{neg} cells of the same brain region.

Morphological phenotype of GFP^{pos} cells of the endopiriform nucleus

Having found that GFP^{pos} EPP neurons were probably glutamatergic, it was of interest next whether these cells would also adopt a more pyramidal cell like morphology. Therefore, biocytin-filled GFP^{pos} cells of the nucleus endopiriformis were reconstructed and their morphometric data were compared to GFP^{neg} cells of the nucleus endopiriformis and to GIN and pyramidal cells of the somatosensory cortex (Table 1). Examples of biocytin-injected cells are shown in Figs. 3a-d. In good agreement with previous reports (Sanchez-Vives et al, 2008), the great majority of biocytin-filled neurons of the endopiriform nucleus (GFP^{pos} and GFP^{neg} neurons) exhibited dendritic spines (Figs. 3a, b). The number of primary processes was similar in all four cells types. However, pyramidal cells exhibited a significantly longer total dendritic length compared to all other cell types (Table 1). Likewise, pyramidal cells had the highest number of dendritic branching points. The number of branching points of the other cell groups was comparable to each other. In comparison to all other cell types, the dendritic complexity was lowest in GIN. Moreover, the total dendritic area in GIN was lower compared to all other cell types. Analysis of the total axonal length revealed that GIN exhibited a significantly greater axonal length compared to GFP^{pos} EPP cells, corroborating the finding that GFP^{pos} EPP cells and GIN of the somatosensory cortex are distinct cell types. Sholl analysis of dendritic processes in turn confirmed the finding that pyramidal cells and GFP^{pos} as well as GFP^{neg} cells of the nucleus endopiriformis exhibited a greater dendritic complexity compared to GIN (Figs. 4a, b). In contrast to that, we observed a significantly larger total axonal length in GIN of the somatosensory cortex compared to GFP^{pos} EPP cells (Table 1) and a greater degree of axonal branching (Figs. 4c, d).

Interestingly, GFP^{pos} and GFP^{neg} cells of the endopiriform nucleus exhibited a similar morphology. Reconstruction of the axon of GFP^{pos} and GFP^{neg} cells of the nucleus

endopiriformis proved to be very challenging as the axon seemed to extend mainly in the z-axis. In agreement with this, robust intranuclear projections along the rostrocaudal axis were reported in neurons of the endopiriform cortex (Behan & Haberly, 1999; Majak & Moryś, 2007; Watson et al., 2017). Therefore, in order to gain further insight into the axonal projections of GFP^{pos} EPP cells, we placed a monopolar stimulation electrode dorsally to the recorded cells into the white matter (distance between recording and stimulating electrode around 500-1000 µm; Fig. 4e). At high stimulation intensities (i.e. 4 - 5 times threshold intensity for the elicitation of a synaptic response), ten out of thirteen GFP^{pos} EPP cells recorded responded with an antidromic spike indicating that the axon also extends dorsally over a long distance (Fig. 4f). Importantly, stimulation at the same location evoked stimulus strength-dependent de- and hyperpolarizing synaptic responses in GFP^{pos} EPP cells (Fig. 4g) suggesting that these cells are integrated into neuronal circuits of this brain region.

Passive membrane properties of GFP^{pos} cells of the endopiriform nucleus

Next, we analyzed the passive membrane properties of GFP^{pos} EPP cells and compared them with those of GFP^{neg} cells of the same brain region and with those of GIN and pyramidal cells of the somatosensory cortex. We found that the mean membrane potential of GIN was significantly lower compared to all other cell types (Fig. 5a). Furthermore, significant differences in the magnitude of the input resistance of the respective cell groups became apparent: GIN exhibited the largest, pyramidal cells the smallest input resistance, GFP^{pos} and GFP^{neg} cells ranged in between these two cell types (Fig. 5b). The input resistance of GFP^{pos} EPP cells was significantly smaller compared to GIN, but did not differ from that of GFP^{neg} cells. In addition, GFP^{pos} cells displayed a significantly larger input resistance than pyramidal cells (Fig. 5b). In addition, we compared the whole cell capacitance of all cell types and, as expected, we found the largest cell capacitance in pyramidal cells followed by cells of the endopiriform nucleus. GIN exhibited the smallest capacitance (Fig. 5c). Analysis of the somatic membrane time constant revealed significant differences between GIN and

pyramidal cells and between GFP^{pos} cells and GIN. Pyramidal cells had the largest membrane time constant, that of GIN was the smallest (Fig. 5d). Analysis of the passive membrane properties revealed that GFP^{pos} EPP cells are distinct from GIN of the somatosensory cortex, but similar to GFP^{neg} cells of the putative nucleus endopiriformis.

GFP^{pos} cells of the nucleus endopirimormis exhibit marked steady-state inward rectification

We next analyzed the current-voltage relationship of all cell types. Examples of representative voltage traces in response to hyper- and depolarizing current injections can be seen in the upper panels of Fig. 6, a and b. The corresponding IV-curves are shown in the lower panels. The quantitative comparison of the current-voltage relationship of the individual cell types encompassed the analysis of the rectification index. All cell types displayed a pronounced steady state inward rectification in the more negative membrane potential ranges. However, the magnitude of rectification was distinct. Pyramidal cells displayed the highest and GIN the smallest rectification index at steady state (Fig. 6c). The rectification ratio of GFP^{pos} EPP cells was significantly different from that of pyramidal neurons. Likewise, GIN displayed a significantly smaller rectification index compared to pyramidal cells. Interestingly, the rectification index of GFP^{pos} EPP cells was significantly smaller compared to that of GFP^{neg} cells of the nucleus endopiriformis (Fig. 6c).

A prominent feature of GIN is a slowly decaying potential sag induced by stronger hyperpolarizing current pulses (Fig. 7c, arrow, Riedemann et al., 2018). A similar but much weaker sag was observed in GFP^{pos} EPP cells (Fig. 7a, asterisk). In order to analyze this phenomenon, the sag amplitude was calculated as the difference between the steady-state membrane potential and the maximum negative peak potential (Figs. 7 a-d). Analysis of the sag potential revealed that GIN had the largest sag potential of all cell groups analyzed (Fig. 7e). No differences were found among the remaining cell groups. In addition, we found that GIN displayed the longest time to the maximal negative voltage deflection compared to all other cell groups analyzed (Fig. 7f). Analysis of the current-voltage relationship of GFP^{pos}

EPP cells in comparison to GFP^{neg} cells and GIN and pyramidal cells of the somatosensory cortex corroborated the finding that GFP^{pos} EPP cells and GIN seem to be two distinct groups of cells and that GFP^{pos} EPP cells seem to be more closely related to pyramidal cells.

Single action potentials kinetics of GFP^{pos} cells resemble those of pyramidal neurons

It was of interest whether the different cell groups also displayed differences in their single action potential kinetics. To this end, we measured the spike amplitude, the spike rising slope and the spike duration of action potentials elicited by just suprathreshold current intensities of GFP^{pos} EPP cells and compared them to the corresponding values of GFP^{neg} cells of the same brain region and to GIN and pyramidal cells of the somatosensory cortex (Fig. 8). We observed differences in the action potential (AP) amplitude and found that GIN displayed the smallest AP amplitude (Fig. 8b). The AP amplitudes of all other cell groups were similar (Fig. 8b). Analysis of the AP rising slope revealed that pyramidal cells exhibited the largest and GFP^{neg} cells the smallest spike velocity and significant differences became only apparent between these two cells groups (Fig. 8c). As expected, GIN displayed the shortest mean AP duration (Fig. 8d). In addition, we found the longest AP duration in GFP^{neg} cells of the EPP, while the AP durations of pyramidal cells and GFP^{pos} EPP cells were similar. In addition, the spike duration of GFP^{neg} cells was significantly longer compared to GFP^{pos} cells of the endopiriform nucleus.

Firing patterns of GFP^{pos} cells of the endopiriform nucleus

Having analyzed single action potential properties, we next investigated the firing patterns in GFP^{pos} EPP cells and compared them to GFP^{neg} cells of the nucleus endopiriformis, to GIN and to pyramidal neurons. We elicited repetitive action potential discharges by injecting current pulses of 1 s in duration and different current strengths, and we qualitatively distinguished between continuous and discontinuous discharge behavior (for definition see Riedemann et al. 2018). Examples of discharges of the different cell types can be seen in Fig. 9a, the corresponding raster plots are depicted in Fig. 9b. All pyramidal cells (100%, i.e.

8 out of 8 cells) and the great majority of GFP^{pos} and GFP^{neg} cells of the endopiriform nucleus (87.2%, i.e. 30 out of 34 cells, resp. 90%, i.e. 18 out of 20 cells) displayed a continuous discharge behavior. In GIN, around 72% of cells displayed a continuous AP discharge pattern (i.e. 10 out of 14). Analysis of the frequency time plots revealed different degrees of frequency adaptation (Fig. 9c). Frequency adaptation was analyzed by comparing the initial frequency (i.e. frequency of the first inter-spike interval, ISI) to the frequency of the second ISI, to the frequency of the mean ISI in the steady state (last 300 ms of a 1 s current pulse) and to the total mean frequency. Generally, GFP^{pos} EPP cells showed the greatest degree of frequency adaptation (Fig. 9c-f). This phenomenon was due to the typical feature of most GFP^{pos} EPP cells to generate initially a doublette of spikes at higher current strengths. Frequency adaptation between the first and second ISI was significantly larger in GFP^{pos} cells compared to GIN (Fig. 9d). No differences were found in the degree of frequency adaptation between the other cell types. Frequency adaptation between the first ISI and the steady state frequency was similar in all cell groups analyzed (Fig. 9e). Likewise, frequency adaptation between the first ISI and the total mean ISI was comparable in all cell groups (Fig. 9f).

In addition, action potential discharge was determined in GFP^{pos} cells at postnatal day 6 (P6) and compared to that of GIN and pyramidal cells of the same age. In support of the immunocytochemical data showing that GFP^{pos} cells neither expressed GAD65/67 nor SOM at P1, we found that the discharge pattern of P6 GFP^{pos} cells was distinct from that of GIN and more closely resembled that of pyramidal neurons (Fig. 10). In addition, single action potential kinetics between pyramidal neurons and GFP^{pos} EPP cells were more similar compared to GIN and GFP^{pos} EPP cells (Fig. 10).

GFP^{pos} cells of the endopiriform nucleus receive spontaneous synaptic input

Given the fact, that GFP^{pos} EPP cells were neither of somatostatinergic nor of GABAergic phenotype, it was of interest, whether they were incorporated into existing neuronal circuits

of the nucleus endopiriformis, i.e. whether they received synaptic input. Therefore, we recorded spontaneous postsynaptic currents (PSCs) in GFP^{pos} EPP cells (Fig. 11a). By using the selective receptor anatgonists Bicuculline ($GABA_A$ receptor) and NBQX (AMPA receptor), we tried to identify the nature of the postsynaptic currents (Figs. 11b and c). We found that GFP^{pos} cells received only sparse synaptic input at a frequency of about 36 events per minute (35.7 ± 42.8 SD; Fig. 11d). The mean amplitude of spontaneous synaptic currents was 13.4 pA (± 3.8 pA SD; Fig. 11e) and the mean duration at half maximal amplitude was 6 ms (± 1.9 ms SD; Fig. 11f). Bath application of Bicuculline resulted in the spontaneous generation of large inward currents probably reflecting paroxysmal depolarizations. This finding indicates that the activity of these cells is controlled by GABAergic inputs (Fig. 11b, left and right panel). Consecutive block of glutamatergic neurotransmission resulted in an almost 100% reduction in the frequency of spontaneous currents (Fig. 11c). The finding that the activity of GFP^{pos} EPP cells was controlled by GABAergic input is further underlined by the finding that we observed spontaneous postsynaptic currents that reversed between a holding potential of -70 mV and -50 mV (Fig. S4).

Discussion

The advent of transgenic animals in which promotor-controlled reporter genes (e.g. eGFP controlled by the GAD67 promotor) are genetically introduced into the genome in order to label certain cell types has greatly facilitated the investigation of even small and rare neuron populations. This approach was of particular importance for the characterization of GABAergic interneurons within the cerebral cortex and for the classification of these cells into three non-overlapping subgroups, i.e.: PV-expressing, SOM-expressing, and 5-HT_3-expressing interneurons (Rudy et al., 2011). Further analysis of one of these subgroups, namely the group of SOM^{pos} INs, revealed subclassifications among populations of genetically labeled cells (Halabisky et al. 2006, Ma et al., 2006; McGarry et al., 2010; Riedemann et al. 2016a, 2018) and, in addition, sporadic reports suggested the possibility of ectopic GFP expression in pyramidal cells instead of GABAergic interneurons in the so-

called GIN mouse line (Ma et al. 2006). In the study presented here, we report on GFP-labeling of non-GABAergic neurons in the so-called GIN mouse line, in which eGFP should be expressed under the control of the GAD67 promotor (Oliva et al., 2000). These GFP^{pos} neurons were located in the nucleus endopiriformis.

The nucleus endopiriformis as that brain structure with the highest density of GFP^{pos} neurons was identified by three different approaches: 1) Anatomical comparison with the corresponding coronal, sagittal and horizontal sections of a stereotactic atlas of the mouse brain (Franklin & Paxinos, 2012), 2) analysis of parvalbumin expression pattern in the claustrum and endopiriform nucleus and 3) by analysis of projections from the cingulate cortex to the nucleus endopiriformis or claustrum via DiI labeling. In agreement with previous reports (Kim, Matney, Roth & Brown, 2016; Real et al., 2003; Smith et al,. 2018; Wójcik et al., 2004), we only found scarce PV immunoreactivity in the area with the highest density of GFP^{pos} neurons, supporting our finding that GFP^{pos} neurons are located within the nucleus endopiriformis. Moreover, analysis of DiI labeling of cingulate cortex projection neurons revealed DiI-positive fibers in close vicinity to GFP^{pos} EPP neurons. Strong connectivity between the cingulate cortex and the claustrum-endopiriform complex was reported previously (Behan & Haberly, 1999; Condé et al., 1995; Qadir et al., 2018; Smith et al., 2018; Wang et al., 2017; Watson et al., 2017; White et al., 2017; Zingg et al., 2018), confirming our observations that these GFP^{pos} neurons are located within the endopiriform nucleus. The endopiriform nucleus is strongly connected to the amygdaloid complex, therefore retrograde labeling of amygdalar projection neurons could further corroborate our finding that GFP^{pos} neurons are located within the endopiriform nucleus (Majak et al., 2002). Netrin-G2 expression as a marker for the mouse nucleus endopiriformis and the claustrum (Wang et al., 2017; Watakabe, Ohsawa, Ichinohe, Rockland & Yamamori, 2014;Yin, Miner & Sanes, 2002; Mathur, Caprioli & Deutch, 2009) was tested. However, in our hands, this approach was not successful. Based on our observations presented here, we report that ectopic GFP labeling of neurons in the so-called GIN mouse results in a systematic delineation of a certain brain structure, in our case the nucleus endopiriformis (see Fig. 1 and Fig. S1).

Identification of the nucleus endopiriformis as brain region with the highest density of GFP^{pos} neurons was followed by a thorough analysis of the neurochemical and electrophysiological properties of GFP^{pos} EPP cells in comparison to cortical GIN and pyramidal neurons.

The first highly surprising finding was that coexpression of GFP and SOM was virtually absent in the GFP^{pos} cells of the nucleus endopiriformis. The absence of coexpression was not due to the absence of SOM^{pos} interneurons in this brain region. In agreement with earlier reports (Eiden, Mezey, Eskay, Beinfeld & Palkovits, 1990), we found that SOM^{pos} neurons were equally distributed within the nucleus endopiriformis and piriform cortex. To our surprise, real GIN represented only a minority of all GFP^{pos} neurons in the nucleus endopiriformis. Previously, Hu et al (2013) described off-target labeling of PV^{pos} interneurons in a SOM-IRES-Cre mouse line (Taniguchi et al., 2011). Although the genetic model is different to a transgenic model, we investigated PV expression in GFP^{pos} cells of the nucleus endopiriformis and found no evidence for PV expression in these cells (see Fig. 2b). In addition, we provided evidence that these GFP^{pos} cells of the nucleus endopiriformis do not express the GABAergic marker enzymes GAD65/67. Instead, the great majority of GFP^{pos} cells contained αCaMKII, a marker enzyme for glutamatergic neurons (McDonald et al., 2002; Wang, Zhang, Szábo & Sun, 2013). We therefore conclude that the GFP^{pos} cells of the nucleus endopiriformis of the GIN mouse line are not GABAergic interneurons, but probably glutamatergic neurons.

In order to substantiate our observation, we performed a morphometric analysis of biocytin-filled GFP^{pos} cells of the nucleus endopiriformis and compared their morphology to that of GIN, pyramidal cells and GFP^{neg} cells of the nucleus endopiriformis. This analysis confirmed the finding that GFP^{pos} cells are a distinct group of cells and that they seem more closely related to pyramidal neurons than to GIN or other interneuron subtypes. The great majority of the GFP^{pos} cells (16 out of 19) exhibited one apical and several basal dendrites (Fig. 3). In good agreement with Sanchez-Vives et al. (2008), spiny dendrites were found in all GFP^{pos} EPP neurons. The axons exited the somata opposite to the apical dendrites and showed only few arborizations. However, the morphometric analysis of cells of the endopiriform nucleus

601 also revealed differences to pyramidal neurons: The directions of the dendrites were not
602 perpendicular to the pia surface, but rather skewed medially. This observation is in good
603 agreement with similar observations made by Wakatabe et al. (2014) in claustral neurons.
604 Given the fact that the claustrum and the nucleus endopiriformis are discussed to be
605 subregions of the same formation (Smith et al., 2018), there is reason to believe that the
606 morphology of GFP^{pos} EPP neurons is similar to that of claustral neurons. Moreover, GFP^{pos}
607 cells were smaller, i.e. they had a smaller total dendritic length and a smaller number of
608 dendritic branching points (Table 1) compared to cortical pyramidal neurons. GFP^{pos} and
609 GFP^{neg} cells in turn seemed to display very similar morphologies. It remains to be
610 investigated, whether GFP^{pos} and GFP^{neg} cells are of the same type or not.
611 Moreover, we elicited synaptic responses in GFP^{pos} neurons of the nucleus endopiriformis by
612 electrical stimulation of the white matter dorsal to the endopiriform nucleus. Generally, the
613 nucleus endopiriformis receives afferent inputs mainly from infralimbic cortical areas and
614 from the entorhinal cortex and it projects back to these brain regions (Behan & Haberly,
615 1999; Lipowska, Kowianski, Majak, Jagalska-Majewska & Morys, 2000; Sugai, Yamamoto,
616 Yoshimura & Kato, 2012; Watson et al., 2017). In addition, the nucleus endopiriformis
617 exhibits robust intranuclear, longitudinal projections along its rostrocaudal axis (Behan &
618 Haberly, 1999; Watson et al., 2017; Zhang et al., 2001). The extranuclear afferent and
619 efferent fibers take their path through the white matter. Stimulation of afferent and efferent
620 fibers of the white matter dorsal of the nucleus endopiriformis elicited putative excitatory and
621 inhibitory synaptic potentials in the GFP^{pos} neurons of the nucleus endopiriformis and, in
622 addition, in about 77% of all neurons investigated, we observed antidromic spikes. In support
623 of this, we found that the axon of GFP^{pos} neurons often exited the endopiriform nucleus in a
624 dorsal direction. The observed synaptic responses possibly originate in the cingulate cortex
625 as we found dense DiI-labeled fibers of cingulate cortex projection neurons in the white
626 matter dorsal of the endopiriform nucleus and within the endopiriform cortex. In the future,
627 electrical stimulation of the cingulum will shed light on the question of whether the evoked
628 synaptic responses after electrical stimulation of the white matter dorsal to the nucleus

endopiriformis indeed originate in the cingulate cortex. By analysis of spontaneous synaptic inputs onto GFP^{pos} EPP neurons we could rule out the hypothesis that these cells are remnants of migrating neurons or dying cells as GFP^{pos} EPP cells are integrated into local circuits of that brain area (Fig. 11 and Fig. S4). In agreement with previous reports (Demir, Haberly & Jackson, 1998; Hoffman & Haberly, 1991, 1996; Sanchez-Vives et al., 2008), we found that the activity of these GFP^{pos} neurons is controlled by inhibitory interneurons as block of GABAergic synaptic transmission elicited paroxysmal depolarizations. In addition, we observed spontaneous postsynaptic currents in GFP^{pos} cells that reversed between -70 mV and -50 mV, indicative of inhibitory currents. Overall, analysis of the electrophysiological properties confirmed the finding that GFP^{pos} cells of the EPP and GIN of the somatosensory cortex are two distinct groups of neurons. In contrast, differences between GFP^{pos} and GFP^{neg} cells of the EPP were small, indicating that both cell groups might be of the same type.

Possible reasons for GFP labeling in pyramidal neurons

In this study, we used the transgenic GIN mouse line and provide evidence for a GAD67 promotor-driven GFP labeling in neurons which do not develop a GABAergic phenotype, but most probably a glutamatergic phenotype. Since we observed this phenomenon in each mouse investigated and always in the same brain area, we can exclude a random false labeling. We also exclude in-house breeding artifacts as this expression was observed over several years and in several generations of animals, including in newly purchased animals. There might be many possible reasons for this systematic false positive labeling. e.g.:

1) A subpopulation of SOM^{pos} interneurons and pyramidal cells are derived from the same progenitor lineage. In light of our findings showing lack of GAD65/67 expression and partial αCaMKII expression in GFP^{pos} EPP neurons at P1, a fate conversion during development seems unlikely (Fig. S3). Noteworthy, αCaMKII expression levels only reach their peak after postnatal day 10 in the mouse hippocampus (Liu et al., 2013) and αCaMKII expression was stronger in the piriform cortex compared to the endopiriform cortex at P1 (Fig. S3). In addition, single action potential kinetics and the action potential discharge patterns in early

postnatal GFP^{pos} EPP cells were more similar to those of cortical pyramidal cells than to those of GIN (Fig. 10).

2) Genes for αCaMKII as well as for GAD67 are transcribed in these cells, however, only the αCaMKII gene is translated. Alternatively, both genes are transcribed and translated, but the degree of GAD translation is minute and therefore cannot be verified immunocytochemically. Indeed, immunocytochemical verification of the GAD65/67 protein is sometimes challenging given the dense GAD65/67^{pos} neuropil. Nonetheless, αCaMKII and GAD65/67 expression in the same cell could not be observed in our hands (Figs. 2c, d).

3) Transcription and translation of GFP in the GIN mouse is dependent on the activation of the promotor region of the GAD67 gene. It is not known how many copies of the transgene have been integrated into the genome and where the copies have been integrated. The possibility exists that local transcription factors, which are only active in this cell population of falsely-labeled GIN, intervene in this process and interact with the GAD67 promotor region, or possibly, directly with the GFP gene and allow its expression.

4) Transcription and translation of genes is a "noisy" process (Sanchez & Golding, 2013) and cell fate specification may underlie mechanisms resembling stochastic resonance (Johnston & Desplan, 2010; Hänggi, 2002; McDonnell & Abbott, 2009). Thus, it might be possible that such mechanisms culminate in GFP^{pos} cells leading to the expression of GFP in non-GABAergic neurons.

In summary, we show here the expression of GFP in excitatory neurons of the nucleus endopiriformis of the GIN mouse line. Ectopic GFP expression in the same mouse line in pyramidal cells has been described by Ma et al. (2006). However, we argue here that this labeling of cells in the nucleus endopiriformis is not random but rather due to intrinsic cell properties of this brain region. In case of a random expression, the pattern of GFP expression would be more dispersed and not highly concentrated in one brain area. It remains to be tested why cells of the nucleus endopiriformis are prone to express GFP. Some studies suggest that the piriform cortex is a neurogenic hub and that these cells,

685 although born prenatally, remain in an undifferentiated state until they mature (Rotheneichner
686 et al., 2018). In line with this idea, we found no evidence for adult neurogenesis in this brain
687 region, neither by adding BrdU (1 mg/ml) to the drinking water for two weeks nor by labeling
688 cells for Ki67 (data not shown). It is possible that the genome of undifferentiated cells is more
689 permissive and more likely to allow transcription and translation. Intriguingly, GFP expression
690 in the nucleus endopiriformis was already observed at postnatal day 1, when cortical GIN
691 were still absent. In light of the observation that these GFP^{pos} cells of the endopiriform
692 nucleus receive synaptic input and project their axons into the white matter, it seems unlikely
693 that the population of GFP^{pos} cells of the nucleus endopiriformis is a "forgotten" group of cells
694 in a "waiting position".
695
696 This study is, to our knowledge, the first to show that GFP labeling results in the delineation
697 of a specific brain region, namely the nucleus endopiriformis. Aside all the genetic problems,
698 which may arise with this observation, this transgenic mouse might turn out to become a
699 valuable model for the investigation of the physiology of the nucleus endopiriformis.
700

701 # References

702 Ascoli G.A., Alonso-Nanclares L., Anderson S.A., Barrionuevo G., Benavides-Piccione R.,
703 Burkhalter A., Buzsaki G., Cauli B., Defelipe J., Fairen A., Feldmeyer D., Fishell G.,
704 Fregnac Y., Freund T.F., Gardner D., Gardner E.P., Goldberg J.H., Helmstaedter M.,
705 Hestrin S., Karube F., Kisvarday Z.F., Lambolez B., Lewis D.A., Marin O., Markram H.,
706 Munoz A., Packer A., Petersen C.C., Rockland K.S., Rossier J., Rudy B., Somogyi P.,
707 Staiger J.F., Tamas G., Thomson A.M., Toledo-Rodriguez M., Wang Y., West D.C.,
708 Yuste R. (2008). Petilla terminology: nomenclature of features of GABAergic
709 interneurons of the cerebral cortex. *Nature Reviews. Neuroscience,* 9(7):557-568.
710 Behan M., Haberly L.B. (1999). Intrinsic and efferent connections of the endopiriform nucleus
711 in rat. *The Journal of Comparative Neurology,* 408(4):532-548.

712 Braak H., Braak E. (1982). Neuronal types in the claustrum of man. *Anatomy and*
713 *Embryology,* (Berl) 163(4):447-60.
714 Condé F., Maire-Lepoivre E., Audinat E., Crépel F. (1995). Afferent connections of the
715 medial frontal cortex of the rat. II. Cortical and subcortical afferents. *The Journal of*
716 *Comparative Neurology,* 352(4):567-93.
717 DeFelipe J., Lopez-Cruz P.L., Benavides-Piccione R., Bielza C., Larranaga P., Anderson S.,
718 Burkhalter A., Cauli B., Fairen A., Feldmeyer D., Fishell G., Fitzpatrick D., Freund T.F.,
719 Gonzalez-Burgos G., Hestrin S., Hill S., Hof P.R., Huang J., Jones E.G., Kawaguchi Y.,
720 Kisvarday Z., Kubota Y., Lewis D.A., Marin O., Markram H., McBain C.J., Meyer H.S.,
721 Monyer H., Nelson S.B., Rockland K., Rossier J., Rubenstein J.L., Rudy B., Scanziani
722 M., Shepherd G.M., Sherwood C.C., Staiger J.F., Tamas G., Thomson A., Wang Y.,
723 Yuste R., Ascoli G.A. (2013). New insights into the classification and nomenclature of
724 cortical GABAergic interneurons. *Nature Reviews. Neuroscience,* 14(3):202-216.
725 Demir R., Haberly L.B., Jackson M.B. (1998). Voltage imaging of epileptiform activity in slices
726 from rat piriform cortex: onset and propagation. *The Journal of Neurophysiology,*
727 80(5):2727-42.
728 Eiden L.E., Mezey E., Eskay R.L., Beinfeld M.C., Palkovits M. (1990). Neuropeptide content
729 and connectivity of the rat claustrum. *Brain Research,* 523(2):245-50.
730 Franklin K.B.J., Paxinos G. (2012). The mouse brain in stereotaxic coordinates, 4th edn.
731 *Academic Press*, San Diego.
732 Gómez-Urquijo S.M., Gutiérrez-Ibarluzea I., Bueno-López J.L., Reblet C. (2000). Percentage
733 incidence of gamma-aminobutyric acid neurons in the claustrum of the rabbit and
734 comparison with the cortex and putamen. *Neuroscience Letters,* 282(3):177-80.
735 Halabisky B., Shen F., Huguenard J.R., Prince D.A. (2006). Electrophysiological
736 classification of somatostatin-positive interneurons in mouse sensorimotor cortex. *The*
737 *Journal of Neurophysiology,* 96(2):834-845.

738 Hänggi P. (2002). Stochastic resonance in biology. How noise can enhance detection of
739 weak signals and help improve biological information processing. *A European Journal*
740 *of Chemical Physics and Physical Chemistry,* 3(3):285-90.
741 Hoffman W.H., Haberly L.B. (1991). Bursting-induced epileptiform EPSPs in slices of piriform
742 cortex are generated by deep cells. *The Journal of Neuroscience,* 11(7):2021-31.
743 Hoffman W.H., Haberly L.B. (1996). Kindling-induced epileptiform potentials in piriform cortex
744 slices originate in the underlying endopiriform nucleus. *The Journal of*
745 *Neurophysiology,* 76(3):1430-8.
746 Hu H., Cavendish J.Z., Agmon A. (2013). Not all that glitters in gold: off-target recombination
747 in the somatostatin-IRES Cre mouse line labels a subset of fast-spiking interneurons.
748 *Frontiers in Neural Circuits,* 7(December):195.
749 Johnston R.J. Jr., Desplan C. (2010). Stochastic mechanisms of cell fate specification that
750 yield random or robust outcomes. *Annual Review of Cell and Developmental Biology,*
751 26:689-719.
752 Kawaguchi Y., Kubota Y. (1996). Physiological and morphological identification of
753 somatostatin- or vasoactive intestinal polypeptide-containing cells among GABAergic
754 cell subtypes in rat frontal cortex. *The Journal of Neuroscience,* 16(8):2701-2715.
755 Kim J., Matney C.J., Roth R.H., Brown S.P. (2016). Synaptic Organization of the Neuronal
756 Circuits of the Claustrum. *The Journal of Neuroscience,* 36(3):773-84.
757 Kinnischtzke A.K., Sewall A.M., Berkepile J.M., Fanselow E.E. (2012). Postnatal maturation
758 of somatostatin-expressing inhibitory cells in the somatosensory cortex of GIN mice.
759 *Frontiers in Neural Circuits,* 6(May):33.
760 Kowiański P., Dziewiatkowski J., Kowiańska J., Moryś J. (1999). Comparative anatomy of the
761 claustrum in selected species: A morphometric analysis. *Brain, Behavior and Evolution,*
762 53(1):44-54.
763 Kowiański P., Moryś J.M., Wójcik S., Dziewiatkowski J., Luczyńska A., Spodnik E.,
764 Timmermans J.P., Moryś J. (2004). Neuropeptide-containing neurons in the

765 endopiriform region of the rat: morphology and colocalization with calcium-binding
766 proteins and nitric oxide synthase. *Brain Research,* 996(1):97-110.
767 Kowiański P., Moryś J.M., Dziewiatkowski J., Wójcik S., Sidor-Kaczmarek J., Moryś J.
768 (2008). NPY-, SOM- and VIP-containing interneurons in postnatal development of the
769 rat claustrum. *Brain Research Bulletin,* 76(6):565-71.
770 Lipowska M., Kowiański P., Majak K., Jagalska-Majewska H., Moryś J. (2000). The
771 connections of the endopiriform nucleus with the insular claustrum in the rat and rabbit.
772 *Folia Morphologica,* (Warsz). 59(2):77-83.
773 Liu W., Chang L., Song Y., Gao X., Ling W., Lu T., Zhang Y., Wu Y. (2013).
774 Immunolocalization of CaMKII and NR2B in hippocampal subregions of rat during
775 postnatal development. *Acta Histochemica,* 115(3):264-72.
776 Ma Y., Hu H., Berrebi A.S., Mathers P.H., Agmon A. (2006). Distinct subtypes of
777 somatostatin containing neocortical interneurons revealed in transgenic mice. *The*
778 *Journal of Neuroscience,* 26(19):5069-5082.
779 Majak K., Kowiański P., Dziewiatkowski J., Karwacki Z., Luczyńska A., Moryś J. (2000).
780 Claustrocingulate connections in the rabbit and rat--a stereological study. *Folia*
781 *Morphologica,* (Warsz). 59(1):47-56.
782 Majak K., Pikkarainen M., Kemppainen S., Jolkkonen E., Pitkänen A. (2002). Projections
783 from the amygdaloid complex to the claustrum and the endopiriform nucleus: a
784 Phaseolus vulgaris leucoagglutinin study in the rat. *The Journal of Comparative*
785 *Neurology,* 451(3):236-49.
786 Majak K., Moryś J. (2007). Endopiriform nucleus connectivities: the implications for
787 epileptogenesis and epilepsy. *Folia Morphologica,* (Warsz). 66(4):267-71.
788 Marx M., Gunter R.H., Hucko W., Radnikow G., Feldmeyer D. (2012). Improved biocytin
789 labeling and neuronal 3D reconstruction. *Nature Protocols,* 7(2):394-407.
790 Mathur B.N. (2014). The claustrum in review. *Frontiers in Systems Neuroscience,* 8(April):48.
791 Mathur B.N., Caprioli R.M., Deutch A.Y. (2009). Proteomic analysis illuminates a novel
792 structural definition of the claustrum and insula. *Cerebral Cortex,* 19(10):2372-9.

McDonald A.J., Muller J.F., Mascagni F. (2002). GABAergic innervation of alpha type II calcium/calmodulin-dependent protein kinase immunoreactive pyramidal neurons in the rat basolateral amygdala. *The Journal of Comparative Neurology,* 446(3):199-218.

McDonnell M.D., Abbott D. (2009). What is stochastic resonance? Definitions, misconceptions, debates, and its relevance to biology. *PLoS Computational Biology,* 5(5):e1000348.

McGarry L.M., Packer A.M., Fino E., Nikolenko V., Sippy T., Yuste R (2010). Quantitative classification of somatostatin-positive neocortical interneurons identifies three interneuron subtypes. *Frontiers in Neural Circuits,* 4(May):12.

Nassar M., Simonnet J., Lofredi R., Cohen I., Savary E., Yanagawa Y., Miles R., Fricker D. (2015). Diversity and overlap of parvalbumin and somatostatin expressing interneurons in mouse presubiculum. *Frontiers in Neural Circuits,* 9(May):20.

Oliva A.A., Jr., Jiang M., Lam T., Smith K.L., Swann J.W. (2000). Novel hippocampal interneuronal subtypes identified using transgenic mice that express green fluorescent protein in GABAergic interneurons. *The Journal of Neuroscience,* 20(9):3354-3368.

Qadir H., Krimmel S.R., Mu C., Poulopoulos A., Seminowicz D.A., Mathur B.N. (2018). Structural Connectivity of the Anterior Cingulate Cortex, Claustrum, and the Anterior Insula of the Mouse. *Frontiers in Neuroanatomy,* 12(November):100.

Real M.A., Dávila J.C., Guirado S. (2003). Expression of calcium-binding proteins in the mouse claustrum. *Journal of Chemical Neuroanatomy,* 25(3):151-60.

Riedemann T., Schmitz C., Sutor B. (2016a). Immunocytochemical heterogeneity of somatostatin-expressing GABAergic interneurons in layers II and III of the mouse cingulate cortex: A combined immunofluorescence/design-based stereologic study. *The Journal of Comparative Neurology,* 524(11):2281-2299.

Riedemann T., Polder H.R., Sutor B. (2016b). Determination and compensation of series resistances during whole-cell patch-clamp recordings using an active bridge circuit and the phase-sensitive technique. *Pflugers Archiv,* 468(10):1725-1740.

820 Riedemann T., Straub T., Sutor B. (2018). Two types of somatostatin-expressing GABAergic
821 interneurons in the superficial layers of the mouse cingulate cortex. *PLoS One,*
822 13(7):e0200567.
823 Rotheneichner P., Belles M., Benedetti B., König R., Dannehl D., Kreutzer C., Zaunmair P.,
824 Engelhardt M., Aigner L., Nacher J., Couillard-Despres S. (2018). Cellular Plasticity in
825 the Adult Murine Piriform Cortex: Continuous Maturation of Dormant Precursors Into
826 Excitatory Neurons. *Cerebral Cortex,* 28(7):2610-2621.
827 Rudy B., Fishell G., Lee S., Hjerling-Leffler J. (2011). Three groups of interneurons account
828 for nearly 100% of neocortical GABAergic neurons. *Developmental Neurobiology,*
829 71(1):45-61.
830 Sanchez A., Golding I. (2013) Genetic determinants and cellular constraints in noisy gene
831 expression. *Science*, 342(6163):1188-93.
832 Sanchez-Vives M.V., Descalzo V.F., Reig R., Figueroa N.A., Compte A., Gallego R. (2008).
833 Rhythmic spontaneous activity in the piriform cortex. *Cerebral Cortex,* 18(5):1179-92.
834 Schreiber S., Samengo I., Herz A.V. (2009). Two distinct mechanisms shape the reliability of
835 neural responses. *The Journal of Neurophysiology,* 101(5):2239-2251.
836 Smith J.B., Alloway K.D., Hof P.R., Orman R., Reser D.H., Watakabe A., Watson G.D.R.
837 (2018). The relationship between the claustrum and endopiriform nucleus: a
838 perspective towards consensus on cross-species homology. *The Journal of*
839 *Comparative Neurology,* doi:10.1002/cne.24537.
840 Sugai T., Yamamoto R., Yoshimura H., Kato N. (2012). Multimodal cross-talk of olfactory and
841 gustatory information in the endopiriform nucleus in rats. *Chemical Senses,* 37(8):681-
842 8.
843 Taniguchi H., He M., Wu P., Kim S., Paik R., Sugino K., Kvitsiani D., Fu Y., Lu J., Lin Y.,
844 Miyoshi G., Shima Y., Fishell G., Nelson S.B., Huang Z.J. (2011). A resource of Cre
845 driver lines for genetic targeting of GABAergic neurons in cerebral cortex. *Neuron,*
846 71(6):995-1013. Erratum in: *Neuron,* (2011). 72(6):1091. Kvitsani, Duda [corrected to
847 Kvitsiani, Duda].

Wang X., Zhang C., Szábo G., Sun Q.Q. (2013). Distribution of CaMKIIα expression in the brain in vivo, studied by CaMKIIα-GFP mice. *Brain Research,* 1518(June):9-25.

Wang Q., Ng L., Harris J.A., Feng D., Li Y., Royall J.J., Oh S.W., Bernard A., Sunkin S.M., Koch C., Zeng H. (2017). Organization of the connections between claustrum and cortex in the mouse. *The Journal of Comparative Neurology,* 525(6):1317-1346.

Watakabe A., Ohsawa S., Ichinohe N., Rockland K.S., Yamamori T. (2014). Characterization of claustral neurons by comparative gene expression profiling and dye-injection analyses. *Frontiers in Systems Neuroscience,* 8(May):98.

Watson C., Puelles L. (2017). Developmental gene expression in the mouse clarifies the organization of the claustrum and related endopiriform nuclei. *The Journal of Comparative Neurology,* 525(6):1499-1508.

Watson G.D.R., Smith J.B., Alloway K.D. (2017). Interhemispheric connections between the infralimbic and entorhinal cortices: The endopiriform nucleus has limbic connections that parallel the sensory and motor connections of the claustrum. *The Journal of Comparative Neurology,* 525(6):1363-1380.

White M.G., Cody P.A., Bubser M., Wang H.D., Deutch A.Y., Mathur B.N. (2017). Cortical hierarchy governs rat claustrocortical circuit organization. *The Journal of Comparative Neurology,* 525(6):1347-1362.

Wójcik S., Dziewiatkowski J., Spodnik E., Ludkiewicz B., Domaradzka-Pytel B., Kowiański P., Moryś J. (2004). Analysis of calcium binding protein immunoreactivity in the claustrum and the endopiriform nucleus of the rabbit. *Acta Neurobiologiae Experimentalis,* (Wars). 64(4):449-60.

Xu X., Roby K.D., Callaway E.M. (2006). Mouse cortical inhibitory neuron type that coexpresses somatostatin and calretinin. *The Journal of Comparative Neurology,* 499(1):144-60.

Xu X., Roby K.D., Callaway E.M. (2010). Immunochemical characterization of inhibitory mouse cortical neurons: three chemically distinct classes of inhibitory cells. *The Journal of Comparative Neurology,* 518(3):389 404.

Yin Y., Miner J.H., Sanes J.R. (2002). Laminets: laminin- and netrin-related genes expressed in distinct neuronal subsets. *Molecular and Cellular Neuroscience,* 19(3):344-58.

Zhang X., Hannesson D.K., Saucier D.M., Wallace A.E., Howland J., Corcoran M.E. (2001). Susceptibility to kindling and neuronal connections of the anterior claustrum. *The Journal of Neuroscience,* 21(10):3674-87.

Zingg B., Dong H.W., Tao H.W., Zhang L.I. (2018). Input-output organization of the mouse claustrum. *The Journal of Comparative Neurology,* 526(15):2428-2443.

Figure Legends

Fig 1 Localization and distribution of GFP^{pos} neurons in the piriform cortex and endopiriform nucleus

a Confocal tile scan (maximum intensity projection) of a coronal brain slice of a P68 GIN mouse with corresponding brain structures according to the *Mouse Brain in Stereotaxic Coordinates* (Franklin & Paxinos, 2012). A dense population of GFP^{pos} cells can be seen in the nucleus endopiriformis. In this study, this population is tentatively designated as

endopiriform population (EPP). **b** Confocal images (maximum intensity projection) of the nucleus endopiriformis. *Left panel:* GFP, *middle panel:* PV, *right panel:* merged image. PV expression is almost absent in the endopiriform nucleus (white ellipse). **c** Confocal images (maximum intensity projection) of the nucleus endopiriformis and piriform cortex. *Left panel:* GFP, *middle panel:* NeuN, *right panel:* merged image. An exemplary counting grid was placed in the merged image. I: sector I, II: sector II, III: sector III. **d** Confocal images (maximum intensity projection) of SOM expression in the piriform cortex and nucleus endopiriformis. *Upper panels:* GFP (green, left) and SOM (magenta, right). *Lower panels:* merged DAPI (left) and merged GFP, SOM and DAPI image (right). **e**, *Left panel:* Coexpression of SOM in GFP^{pos} cells in sectors I, II and III of the nucleus endopiriformis and piriform cortex (n=4 animals). *Right panel:* Coexpression of GFP in SOM^{pos} interneurons in sectors I, II and III of the nucleus endopiriformis and piriform cortex (n=4 animals). All scale bars: 100 µm.

Fig 2 Neurochemical profile of GFP^{pos} EPP cells

a Confocal images (maximum intensity projection) of GFP^{pos} EPP cells taken with a 40× water objective. The cells were stained for GFP (green), SOM (white) and DAPI (blue). The merged image is shown in the right panel. Colocalization of GFP and SOM fluorescence is virtually absent. **b** Confocal images (maximum intensity projection) of GFP^{pos} EPP cells. The cells were labeled for GFP (green), PV (magenta) and DAPI (blue). The merged image is shown in the right panel. **c** Confocal images (maximum intensity projection) of cells in the nucleus endopiriformis stained for GFP (green), GAD65/67 (magenta) and αCaMKII (white). The merged image (with DAPI in blue) is shown in the right panel. Light grey arrows indicate $GAD65/67^{pos}$ cells. **d** Confocal images (maximum intensity projection) of cells in the piriform cortex stained for GFP (green), GAD65/67 (magenta) and αCaMKII (white). The merged image (with DAPI in blue) is shown in the right panel. Solid arrows indicate $GAD65/67^{pos}$ cells. Open arrows indicate GFP^{pos} and $GAD65/67^{pos}$ cells. All scale bars: 20 µm.

Fig 3 Morphology of GFP^{pos} EPP cells

a, *left panels* Confocal z-stack images as maximum intensity projections of representative GFP^{pos} cells of the nucleus endopiriformis. Insets: Dendritic spines on the corresponding cells. Scalebar: 10 µm. *Middle panels* Low magnification confocal images (maximum intensity projection) of the biocytin-filled cells shown in the left panels. Green: GFP, white: biocytin-filled neuron. *Right panels* Polar histograms of the corresponding biocytin-filled neurons shown in the left panels. **b**, *left panels* Confocal z-stack images as maximum intensity projections of representative GFP^{neg} cells of the nucleus endopiriformis with spiny dendrites (insets, scalebar: 10 µm). *Middle panels* Low magnification confocal images (maximum intensity projection) of the biocytin-filled cells shown in the left panels. Green: GFP, white: biocytin-filled neuron. *Right panels* Polar histograms of the corresponding biocytin-filled neurons shown in the left panel. **c** Confocal z-stack images as maximum intensity projections of a representative GIN of the somatosensory cortex. **d** Confocal z-stack images as maximum intensity projections of a representative pyramidal cell of the somatosensory cortex in high (left panel) and low (right panel) magnification. All scale bars but those in insets: 100 µm.

Fig 4 Morphometric analysis of GFP^{pos} EPP cells

a Sholl analysis of dendritic length in GFP^{pos} and GFP^{neg} cells, GIN and pyramidal neurons. The dendritic length is plotted as a function of the Sholl distance (mean ± SEM). **b** Number of dendritic intersections plotted as a function of the Sholl distance (mean ± SEM). **c** Sholl analysis of axon length in GFP^{pos} cells and in GIN. The axon length is plotted as a function of the Sholl distance (mean ± SEM). Compared to GFP^{pos} cells, we found a greater axonal length in GIN (130 µm: $p<0.05$; 150 µm: $p<0.05$; 170 µm: $p<0.05$; 190 µm: $p<0.05$; 210 µm: $p<0.01$; 230 µm: $p<0.001$; 250 µm: $p<0.001$; ANOVA two-way analysis of variance). **d** Number of axonal intersections plotted as a function of the Sholl distance (mean ± SEM). Compared to GFP^{pos} cells, we found a greater degree of axonal branching in GIN (110 µm: $p<0.001$; 130 µm: $p<0.01$; 150 µm: $p<0.001$; 170 µm: $p<0.001$; 190 µm: $p<0.001$; 210 µm:

959 p<0.001; 230 µm: p<0.001; 250 µm: p<0.001; 270 µm: p<0.05; ANOVA two-way analysis of
960 variance). **e** Coronal brain section depicting the stimulation site for the induction (arrow) of
961 evoked responses of GFP^{pos} EPP cells. **f** Five evoked responses at a stimulation intensity of
962 500 µA are superimposed. Black traces indicate responses where an antidromic spike was
963 triggered, the light grey trace indicates a synaptic response without antidromic spike. **g**
964 Exemplary evoked responses in a GFP^{pos} cell after stimulations with current intensities
965 ranging between 50 and 500 µA. Action potentials are truncated. Note: hyperpolarizing
966 responses (putatively inhibitory postsynaptic potentials) are preceded by fast-rising excitatory
967 potentials.
968
969 **Fig 5 Passive membrane properties of GFP^{pos} EPP cells**
970 **a** Scatter plot of the resting membrane potentials (RMP) of GFP^{pos} and GFP^{neg} cells of the
971 nucleus endopiriformis and of GIN and pyramidal cells (PC) of the somatosensory cortex
972 (mean ± SD). GFP^{pos}: -71.0 mV ± 5.2 mV; GFP^{neg}: -71.0 mV ± 5.9 mV; GIN: -66.3 mV± 4.1
973 mV; PC: -69.4 mV ± 5.8 mV (GFP^{pos} vs. GIN, p<0.01; GFP^{neg} vs. GIN, p<0.01; One-way
974 ANOVA with Bonferroni's multiple comparison). **b** Scatter plot (with means ± SD) showing
975 the input resistance of GFP^{pos}, GFP^{neg} cells in comparison to GIN and pyramidal cells (PC).
976 GFP^{pos}: 249.1 MΩ ± 104.6 MΩ; GFP^{neg}: 288.0 MΩ ± 128.4 MΩ; GIN: 405.8 MΩ ± 180.5 MΩ;
977 PC: 127.4 MΩ ± 58.4 MΩ (GFP^{pos} vs. GIN, p<0.01; GFP^{pos} vs. PC, p<0.01; GFP^{neg} vs. PC,
978 p<0.001; GIN vs. PC, p<0.001, Kruskal-Wallis test with Dunn's multiple comparison). **c**
979 Scatter plot showing the apparent whole-cell capacitance of GFP^{pos}, GFP^{neg} cells in
980 comparison to GIN and pyramidal cells (PC). GFP^{pos}: 120.5 pF ± 28.7 pF; GFP^{neg}: 118.7 pF ±
981 43.8 pF; GIN: 97.5 ± 24.6 pF; PC: 182.5 pF ± 69.0 pF (GFP^{pos} vs. GIN, p<0.05; GFP^{pos} vs.
982 PC, p<0.05; GFP^{neg} vs. PC, p<0.05; GIN vs. PC, p<0.001, Kruskal-Wallis test with Dunn's
983 multiple comparison). **d** The somatic membrane time constant of the respective cell groups
984 (GFP^{pos}, GFP^{neg}, GIN and (PC) depicted as a scatter plot. GFP^{pos}: 26.5 ms ± 7.5ms; GFP^{neg}:
985 26.7 ms ± 11.5 ms; GIN: 34.8 ms ± 15.2 ms; PC: 21.6ms ± 10.9 ms (GFP^{pos} vs. GIN, p<0.05;
986 GIN vs. PC, p<0.01, One-way ANOVA with Bonferroni's multiple comparison.

Figure 6 Analysis of the current-voltage relationship in GFP^{pos} EPP cells

a, **b**, *upper panel* Exemplary voltage traces of a GFP^{pos} EPP cell and a GIN upon injection of a series of hyper- and depolarizing current pulses. The solid line in (a) indicates the point of measurement of the steady state potential, the dashed line indicates that of the initial membrane potential. The corresponding current-voltage plots are shown in the *lower panels*. Solid circles indicate the steady state, open circles indicate the initial value. **c** The rectification ratio at a membrane potential of -100 mV in the individual cell groups is depicted as a scatter plot. GFP^{pos}: 1.7 ± 0.38; GFP^{neg}: 2.0 ± 0.51; GIN: 1.44 ± 0.23; PC: 2.44 ± 0.62 (GFP^{pos} vs. GIN, p<0.001; GFP^{neg} vs. GIN, p<0.001; GIN vs. PC, p<0.001, Kruskal-Wallis test with Dunn's multiple comparison).

Figure 7 GFP^{pos} EPP cells exhibit a small sag potential with a fast onset

a-**d** Exemplary voltage traces of a GFP^{pos} EPP cell, a GFP^{neg} cell of the nucleus endopiriformis, a GIN and a pyramidal cell upon injection of a hyperpolarizing current pulse. The asterisk in (a) indicates the time point of the maximal negative membrane potential, the arrow in (c) indicates the sag potential determined at the end of the pulse. **e** Comparison of the sag potential in the different cell groups (GFP^{pos}, GFP^{neg}, GIN and PC). The magnitudes of the sag potentials are depicted as a scatter plot. GFP^{pos}: 3.74 mV ± 1.53 mV; GFP^{neg}: 2.52 mV ± 1.81 mV; GIN: 8.85 mV ± 3.82 mV; PC: 3.41 mV ± 3.1 mV (GFP^{pos} vs. GIN, p<0.001; GFP^{neg} vs. GIN, p<0.001; GIN vs. PC, p<0.001, Kruskal-Wallis test with Dunn's multiple comparison). **f** Comparison of the time to the negative peak in the different cell groups (GFP^{pos}, GFP^{neg}, GIN and PC) shown as a scatter plot. GFP^{pos}: 65.3 ms ± 19.6 ms; GFP^{neg}: 61.2 ms ± 12.6 ms; GIN: 110.5 ms ± 44.6 ms; PC: 48.3 ms ± 29.2 ms (GFP^{pos} vs. GIN, p<0.001; GFP^{neg} vs. GIN, p<0.001; GIN vs. PC, p<0.001, Kruskal-Wallis test with Dunn's multiple comparison).

Figure 8 Action potential properties of GFP^{pos} EPP cells

a, *left panel* Representative action potential elicited by a 50 ms lasting current ramp. *Right panel* First derivative of the corresponding action potential. **b** Scatter plot showing the action potential (AP) amplitudes in the different cell groups (with means ± SD). GFP^{pos}: 98.3 mV ± 9.7 mV; GFP^{neg}: 96.2 mV ± 13.9 mV; GIN: 77.8 mV ± 8.2 mV; PC: 98.0 mV ± 14.2 mV (GFP^{pos} vs. GIN, $p<0.001$; GFP^{neg} vs. GIN, $p<0.001$; PC vs. GIN, $p<0.001$, One-way ANOVA with Bonferroni's multiple comparison). **c** Scatter plot showing the AP rising slope of the individual cell groups. GFP^{pos}: 169.6 V/s ± 43.7 V/s; GFP^{neg}: 146.5 V/s ± 44.6 V/s; GIN: 152.2 V/s ± 38.6V/s; PC: 192.4 V/s ± 63.9 V/s (GFP^{neg} vs. PC, $p<0.05$; One-way ANOVA with Bonferroni's multiple comparison. **d** Scatter plot showing the AP durations in the different cell groups. GFP^{pos}: 1.40 ms ± 0.3 ms; GFP^{neg}: 1.67 ms ± 0.26 ms; GIN: 0.92 ms ± 0.15 ms; PC: 1.33ms ± 0.29 ms (GFP^{pos} vs. GFP^{neg}, $p<0.001$; GFP^{pos} vs. GIN, $p<0.001$; GFP^{pos} vs. GIN, $p<0.001$; GFP^{neg} vs. PC, $p<0.01$; GIN vs. PC, $p<0.001$, One-way ANOVA with Bonferroni's multiple comparison).

Fig 9 Action potential firing patterns in GFP^{pos} EPP cells

a Examplary AP discharges in GFP^{pos}, GFP^{neg} cells of the nucleus endopiriformis compared to GIN and pyramidal cells of the somatosensory cortex. **b** Corresponding raster plots of the cells depicted in (a). Each dot indicates an action potential, each row indicates a train of action potential at a given current intensity. **c** Corresponding frequency-time plots of the cells depicted in (a). **d** Scatter plot (means ± SD) displaying the ISI_1:ISI_2 ratio in the different cell groups. GFP^{pos}: 2.50 ± 1.31; GFP^{neg}: 2.05 ± 1.67; GIN: 1.32 ± 0.21; PC: 1.56 ± 0.37 (GFP^{pos} vs. GIN, $p<0.05$; Kruskal-Wallis test with Dunn's multiple comparison). **e** ISI_1: ISI_{stst} ratio depicted as scatter plot. GFP^{pos}: 5.82 ± 4.80; GFP^{neg}: 3.40 ± 3.20; GIN: 5.00 ± 3.12; PC: 2.45 ± 0.80. **f** ISI_1: $ISI_{totalmean}$ ratio depicted as scatter plot. GFP^{pos}: 3.00 ± 1.46; GFP^{neg}: 2.06 ± 1.39; GIN: 2.26 ± 0.63; PC: 1.83 ± 0.50.

Fig. 10 Action potential discharge in early postnatal GFP^{pos} EPP cells *Left panel* Action potential discharge pattern of a GFP^{pos} EPP cell (**a**) compared to that of a GIN of the anterior

cingulate cortex (ACC, **b**) and that of a pyramidal neuron of the frontal cortex (**c**) at postnatal day 6. Resting membrane potential (RMP) GFP^{pos} neuron: -68 mV; RMP GIN: -69 mV, RMP pyramidal cell: -62 mV. Input resistance (R_N) GFP^{pos} neuron: 1294 MΩ; R_N GIN: 714 MΩ, R_N pyramidal cell: 1350 MΩ. *Right panel* The second spike of the train of action potentials from the corresponding cells on the left is depicted at a higher temporal resolution.

Fig 11 GFP^{pos} EPP cells receive spontaneous synaptic input

a, *left panel* Representative 5 min lasting recordings of spontaneous synaptic activity in GFP^{pos} EPP cells under control conditions. *Right panel* All individual postsynaptic currents (PSCs) of the corresponding recording shown in (a) are depicted as light grey traces, the black traces indicates the averaged response. **b,** *left panel* A 5 min lasting recording of the same cell depicted in (a) is shown after bath application of 10 µM Bicuculline. *Right panel* Current trace within the rectangle shown on an expanded scale in the left panel. **c** Continued recording of the same cell depicted in (a) and (b) after perfusion with 10 µM NBQX. Scatter plots (mean ± SD) depicting the PSC frequency ([per min] **d**), the PSC amplitude (**e**) and the PSC duration (**f**) in GFP^{pos} cells under control conditions.

Supporting Information

S1 Photomicrograph of a horizontal brain slice of a P1 and P37 GIN mouse (upper panel). Photomicrograph of a saggital brain slice of a P37 GIN mouse (lower panel) with corresponding brain structures according to the *Mouse Brain in Stereotaxic Coordinates* (Franklin & Paxinos, 2012). The dense cluster of GFP^{pos} cells in the deeper brain nuclei corresponding to the nucleus endopiriformis can be seen.

S2 Connectivity between the cingulate cortex and claustrum-endopiriform complex. Photomicrographs of two coronal brain slices of the same animal depicting the injection site of the DiI crystal in the cingulate cortex (**a**). The open ellipse represents that brain region with the highest density of GFP^{pos} neurons, i.e. the nucleus endopiriformis. As can be seen from

the images in (**b**) and (**c**) from the same animal, GFP^{pos} EPP neurons and DiI-positive fibers are in close vicinity to each other. All scalebars: 50 µm.

S3 Confocal z-stack images as maximum intensity projections of representative GFP^{pos} cells of the nucleus endopiriformis at postnatal day 1 (P1) taken with a 40× water objective. **a** The cells were stained for GFP (green), SOM (magenta) and GAD65/67 (white). The merged image is shown in the right panel. Colocalization of GFP, SOM and GAD65/67 fluorescence is virtually absent. The open arrow indicates a SOM^{pos} IN that also expresses GAD65/67. **b** The cells were labeled for GFP (green), αCaMKII (magenta) and GAD65/67 (white). The merged image is shown in the right panel. The open arrow indicates a GFP^{pos} neuron that expresses αCaMKII but lacks GAD65/67 expression. **c** Confocal images (maximum intensity projection) of cells in the nucleus endopiriformis stained for GFP (green), αCaMKII (magenta) and GAD65/67 (white). The open arrows indicate αCaMKII-expressing GFP^{pos} neurons. αCaMKII expression levels are higher in the piriform cortex at that age. All scale bars: 20 µm.

S4 Spontaneous synaptic currents recorded in GFP^{pos} EPP neurons at a holding potential of -70 mV and at a holding potential of -50 mV.

Figure 1

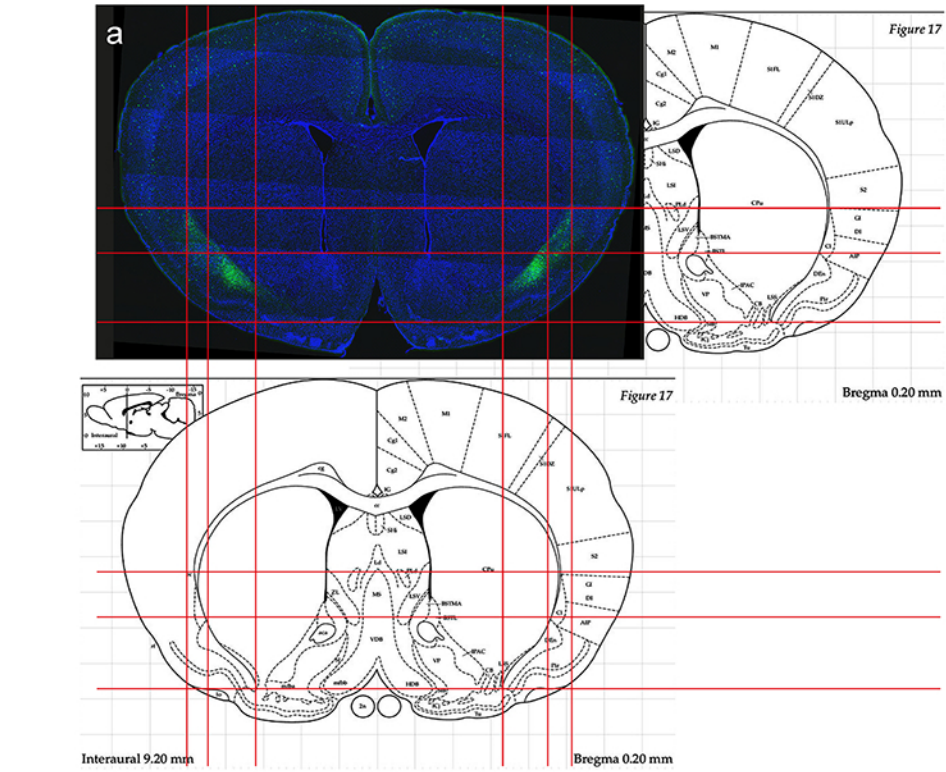
a
Figure 17
Bregma 0.20 mm
Figure 17
Interaural 9.20 mm
Bregma 0.20 mm

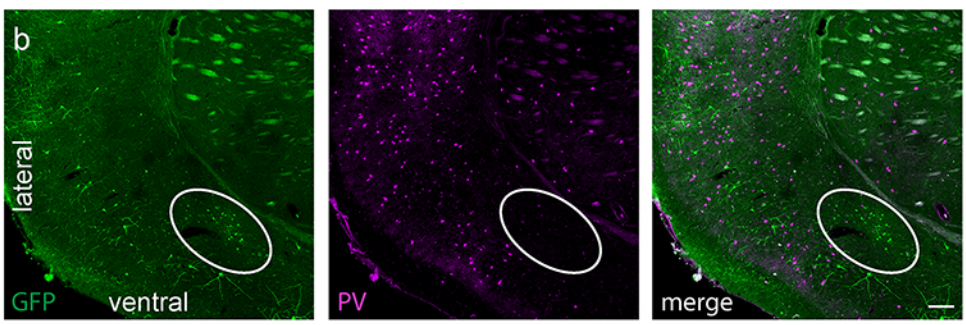
b
lateral
GFP
ventral
PV
merge

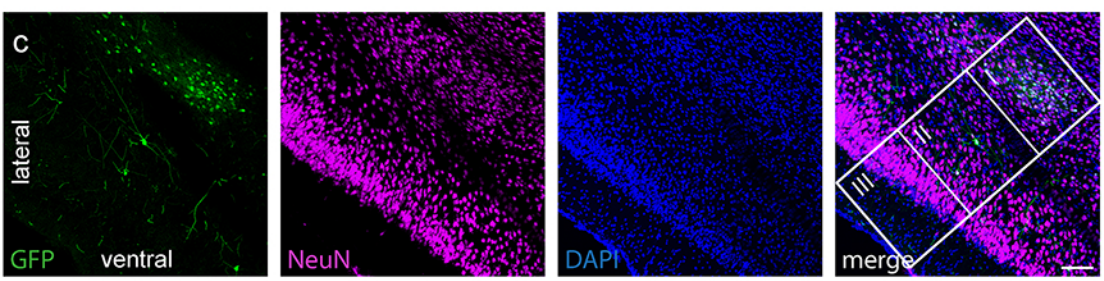
c
lateral
GFP
ventral
NeuN
DAPI
merge

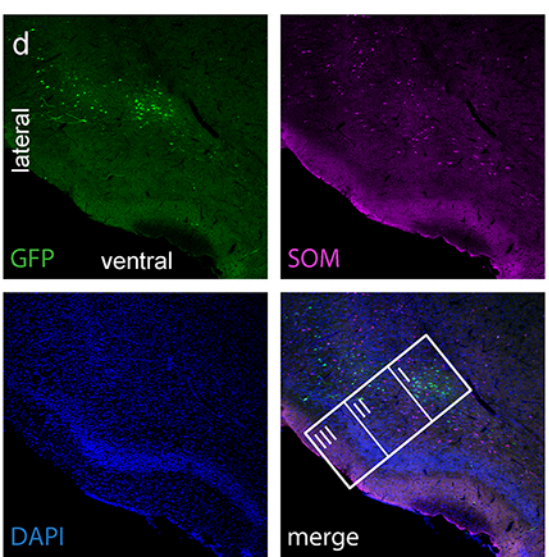
d
lateral
GFP
ventral
SOM
DAPI
merge

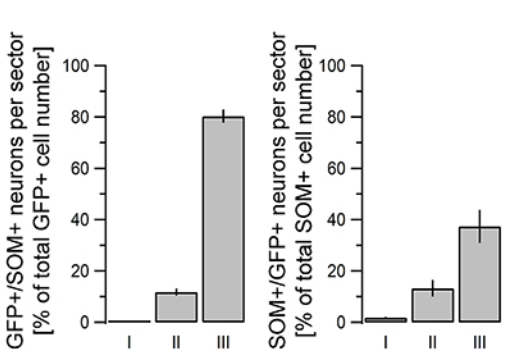
e
GFP+/SOM+ neurons per sector
[% of total GFP+ cell number]
100
80
60
40
20
0
I
II
III
SOM+/GFP+ neurons per sector
[% of total SOM+ cell number]
100
80
60
40
20
0
I
II
III

Figure 2

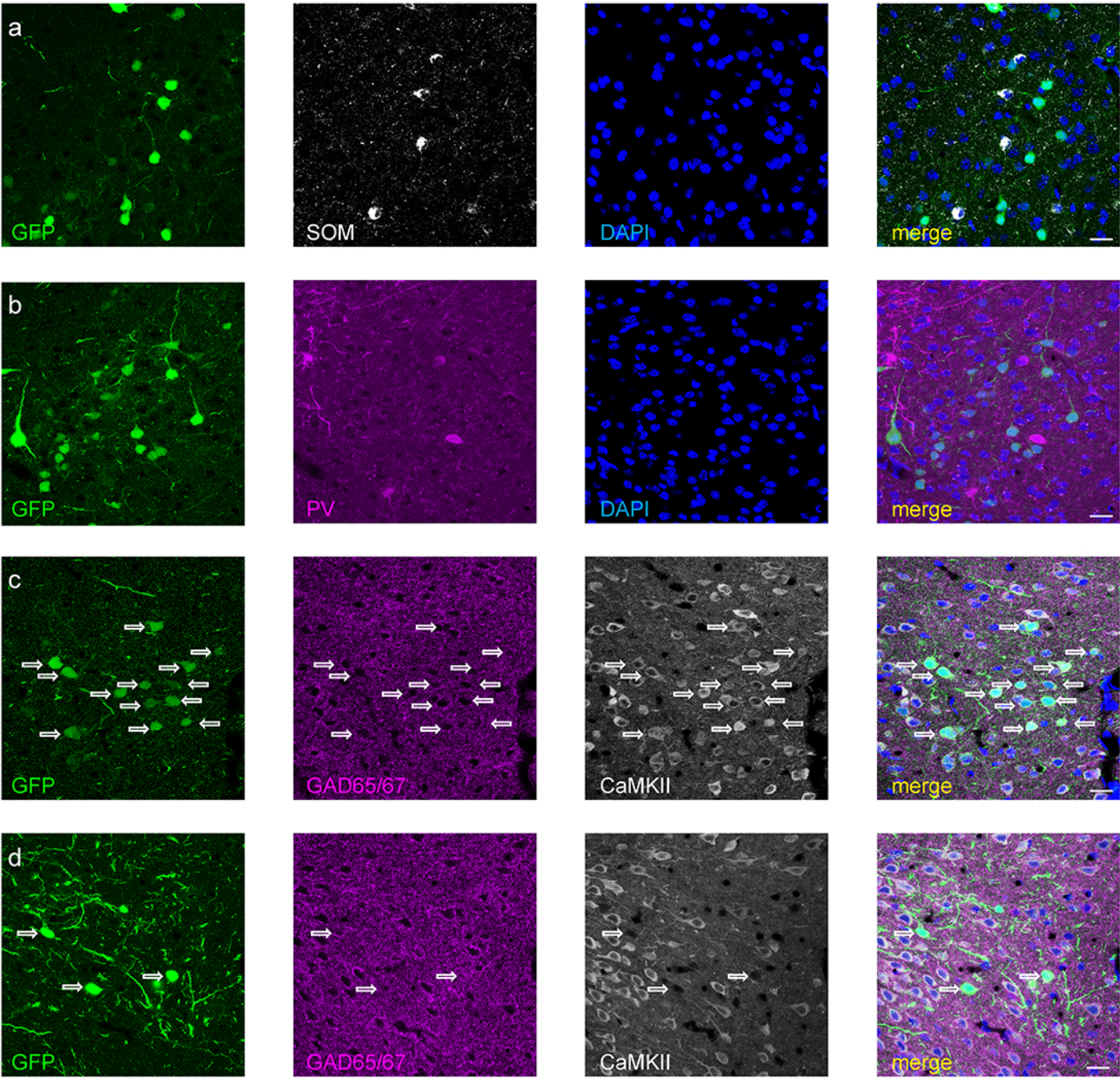
a
GFP
SOM
DAPI
merge
b
GFP
PV
DAPI
merge
c
GFP
GAD65/67
CaMKII
merge
d
GFP
GAD65/67
CaMKII
merge

Figure 3

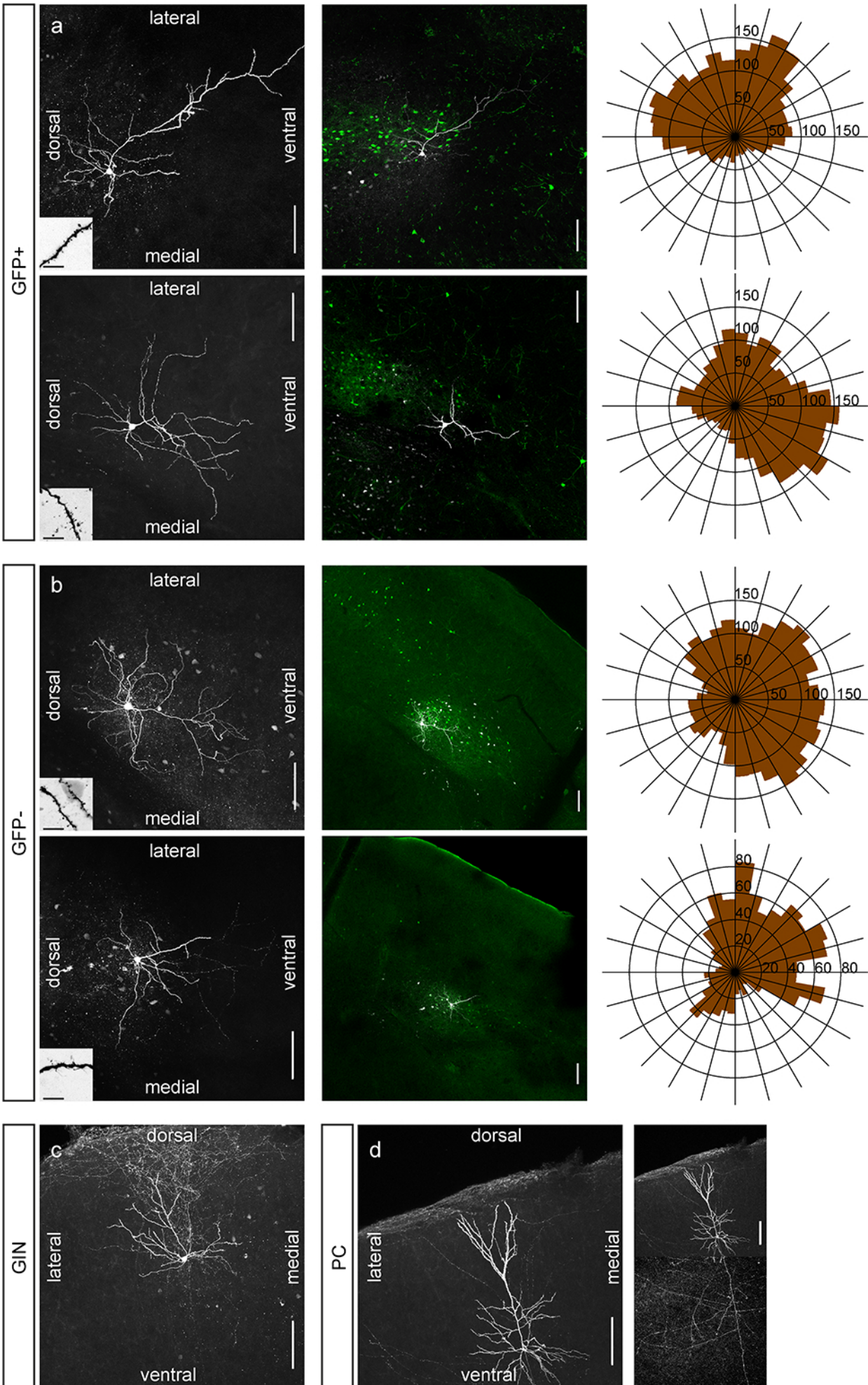
GFP+
GFP-
GIN
PC
a
b
c
d
lateral
medial
dorsal
ventral
150
100
50
80
60
40
20

Figure 4

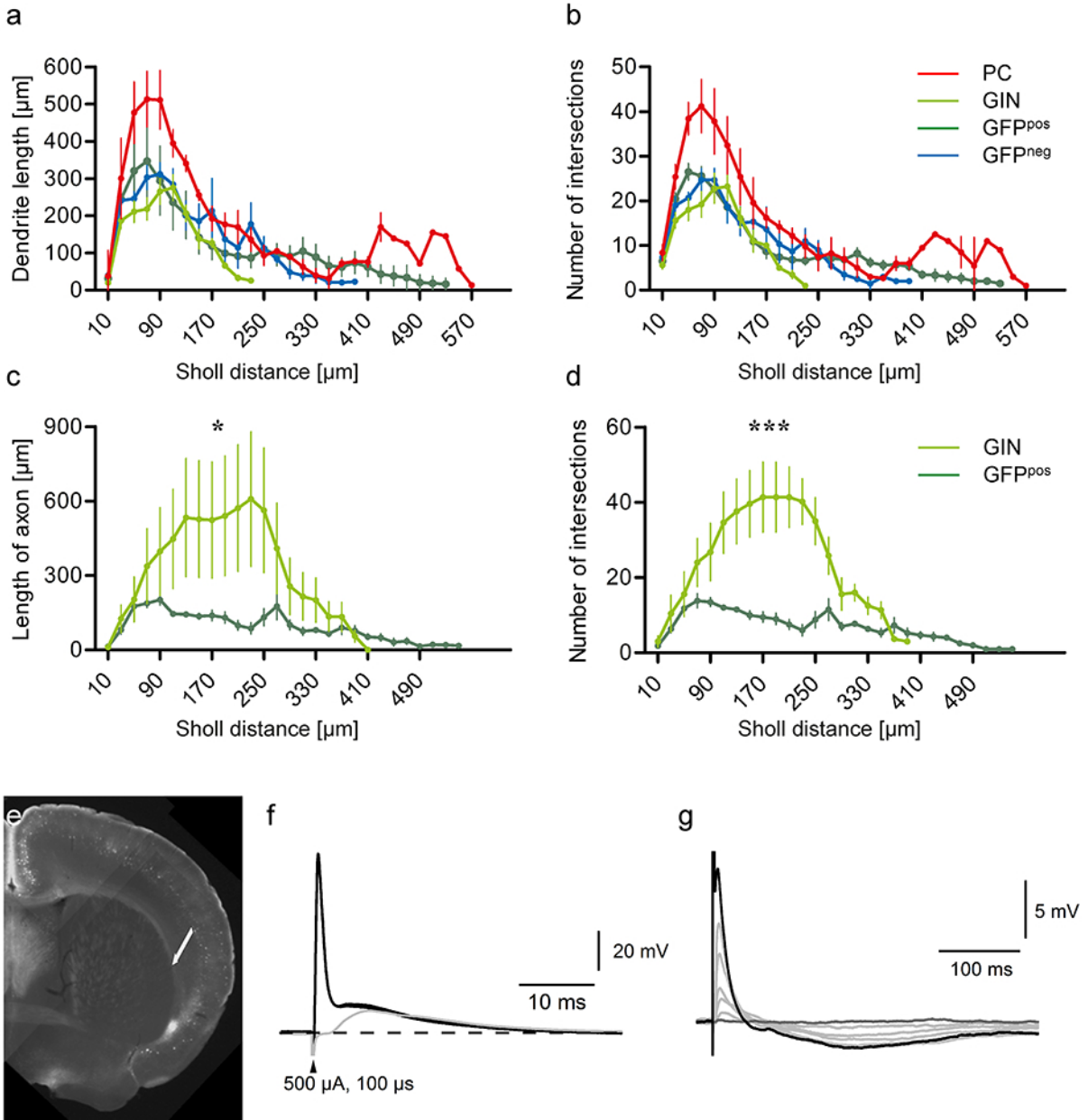
a
Dendrite length [µm]
600
500
400
300
200
100
0
10
90
170
250
330
410
490
570
Sholl distance [µm]
b
Number of intersections
50
40
30
20
10
0
PC
GIN
GFPpos
GFPneg
Sholl distance [µm]
c
Length of axon [µm]
900
600
300
0
*
Sholl distance [µm]
d
Number of intersections
60
40
20
0
***
GIN
GFPpos
Sholl distance [µm]
e
f
20 mV
10 ms
500 µA, 100 µs
g
5 mV
100 ms

Figure 5

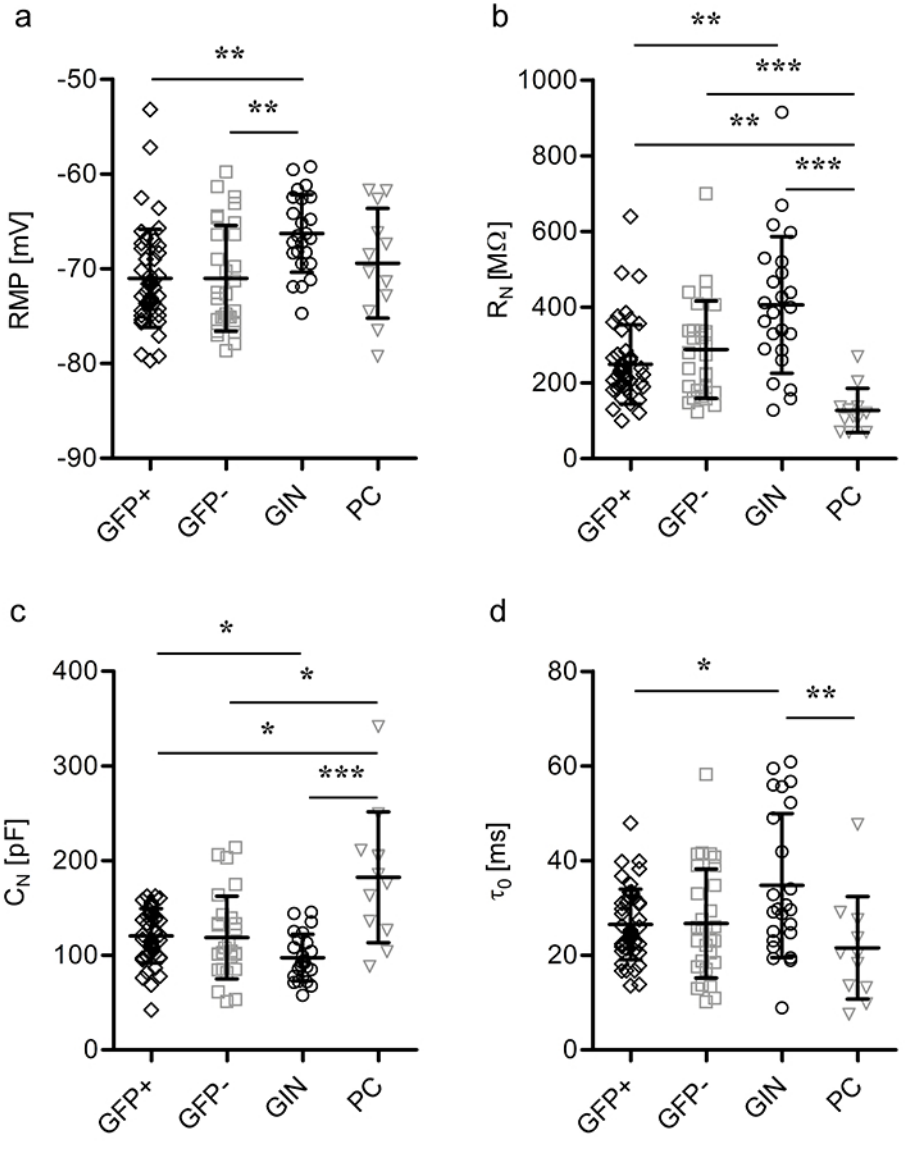

Figure 6

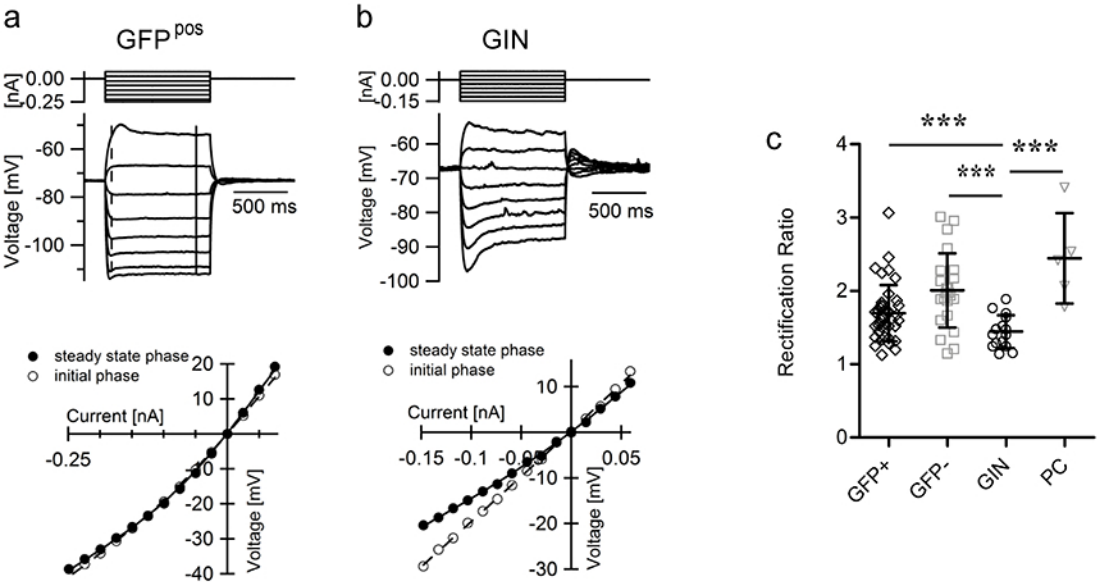
a
GFP pos
[nA] 0.00
0.25
-60
-80
-100
Voltage [mV]
500 ms
steady state phase
initial phase
Current [nA]
-0.25
20
10
-10
-20
-30
-40
Voltage [mV]
b
GIN
[nA] 0.00
-0.15
-60
-70
-80
-90
-100
Voltage [mV]
500 ms
steady state phase
initial phase
Current [nA]
-0.15
-0.1
0.05
10
-10
-20
-30
Voltage [mV]
c
***
***
***
Rectification Ratio
4
3
2
1
0
GFP+
GFP-
GIN
PC

Figure 7

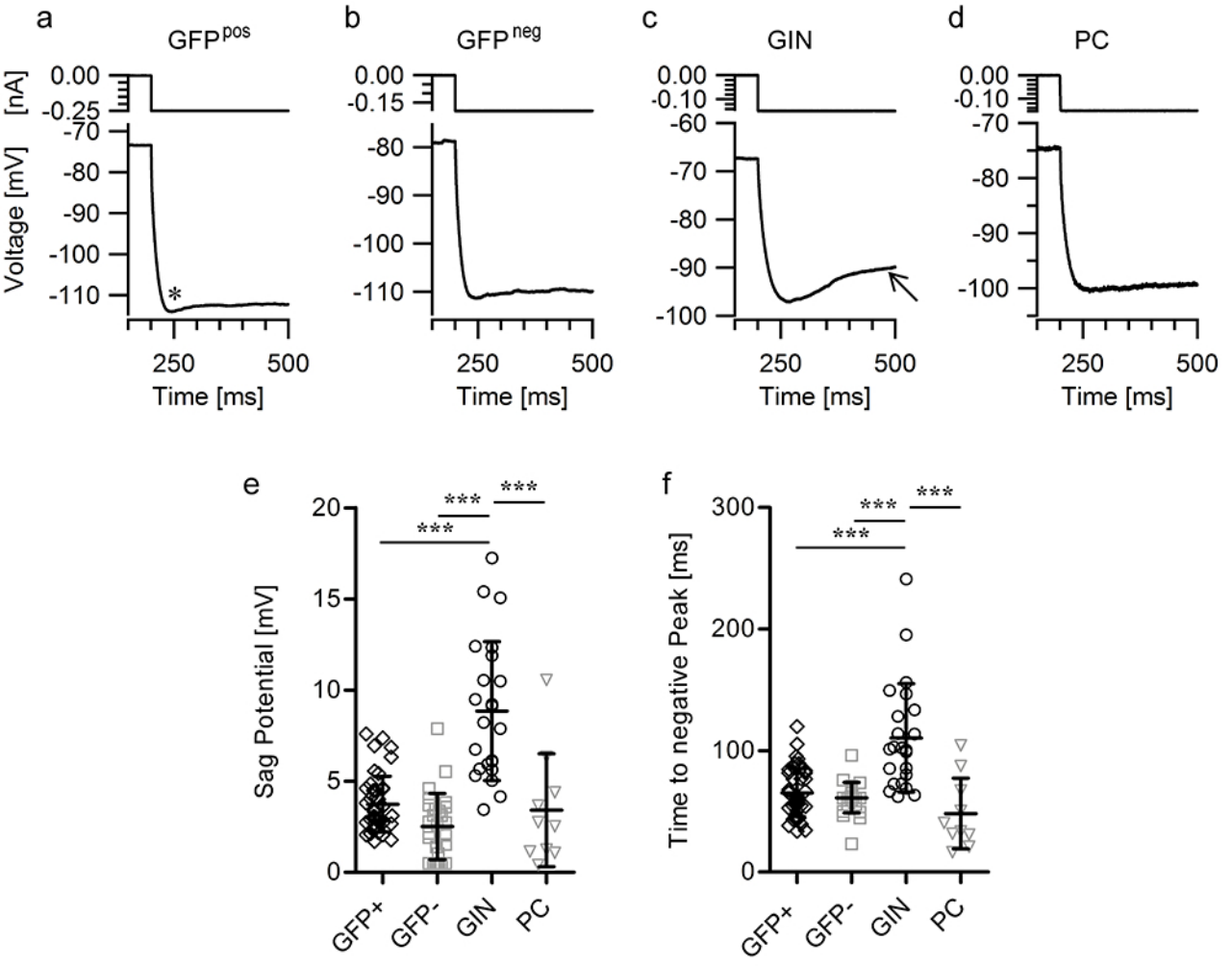
a
GFP pos
b
GFP neg
c
GIN
d
PC
Voltage [mV]
[nA]
0.00
-0.25
-0.15
-0.10
-70
-80
-90
-100
-110
-60
*
250
500
Time [ms]
e
Sag Potential [mV]
20
15
10
5
0
***
f
Time to negative Peak [ms]
300
200
100
GFP+
GFP-
GIN
PC

Figure 8

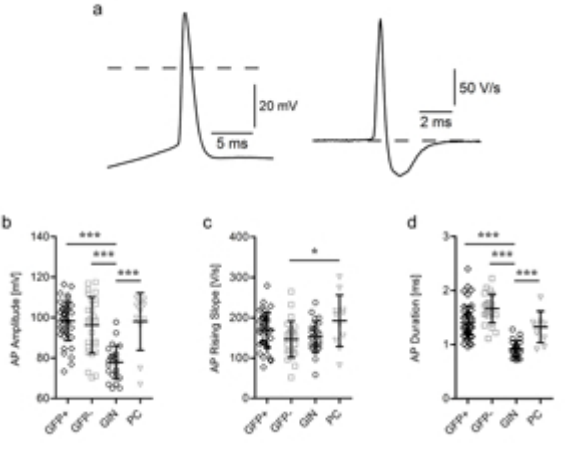
a
20 mV
5 ms
50 V/s
2 ms
b
AP Amplitude [mV]
***
***
***
GFP+
GFP-
GIN
PC
c
AP Rising Slope [V/s]
*
d
AP Duration [ms]
***
***
***

Figure 9

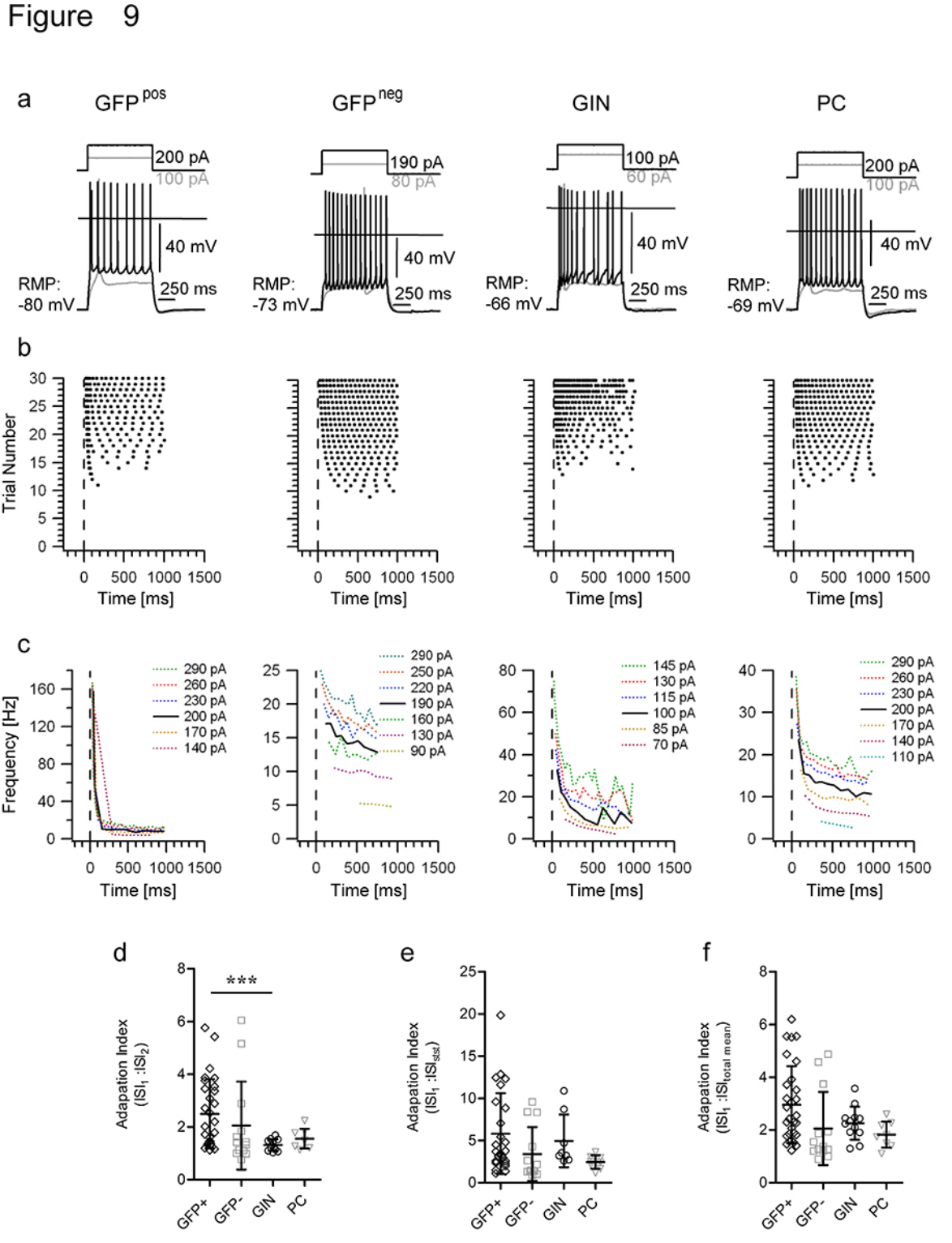
a
GFP pos
GFP neg
GIN
PC
200 pA
100 pA
190 pA
80 pA
100 pA
60 pA
200 pA
100 pA
40 mV
250 ms
RMP:
-80 mV
RMP:
-73 mV
RMP:
-66 mV
RMP:
-69 mV
b
Trial Number
Time [ms]
c
Frequency [Hz]
290 pA
260 pA
230 pA
200 pA
170 pA
140 pA
250 pA
220 pA
190 pA
160 pA
130 pA
90 pA
145 pA
130 pA
115 pA
100 pA
85 pA
70 pA
110 pA
d
e
f
Adapation Index
(ISI1 :ISI2)
(ISI1 :ISIstst)
(ISI1 :ISItotal mean)
***
GFP+
GFP-
GIN
PC

Figure 10

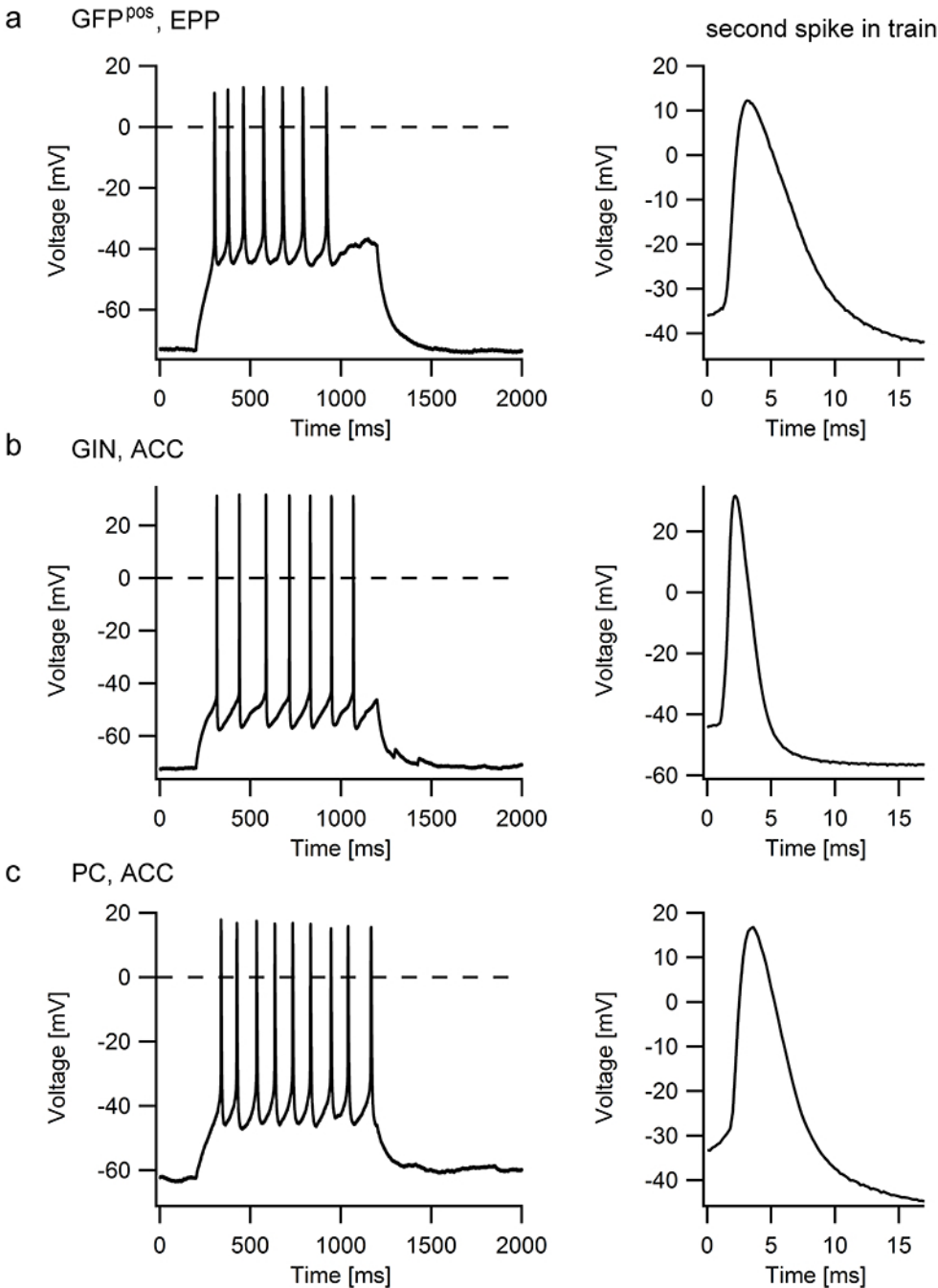
a
GFP^{pos}, EPP
second spike in train
Voltage [mV]
Time [ms]
b
GIN, ACC
c
PC, ACC

Figure 11

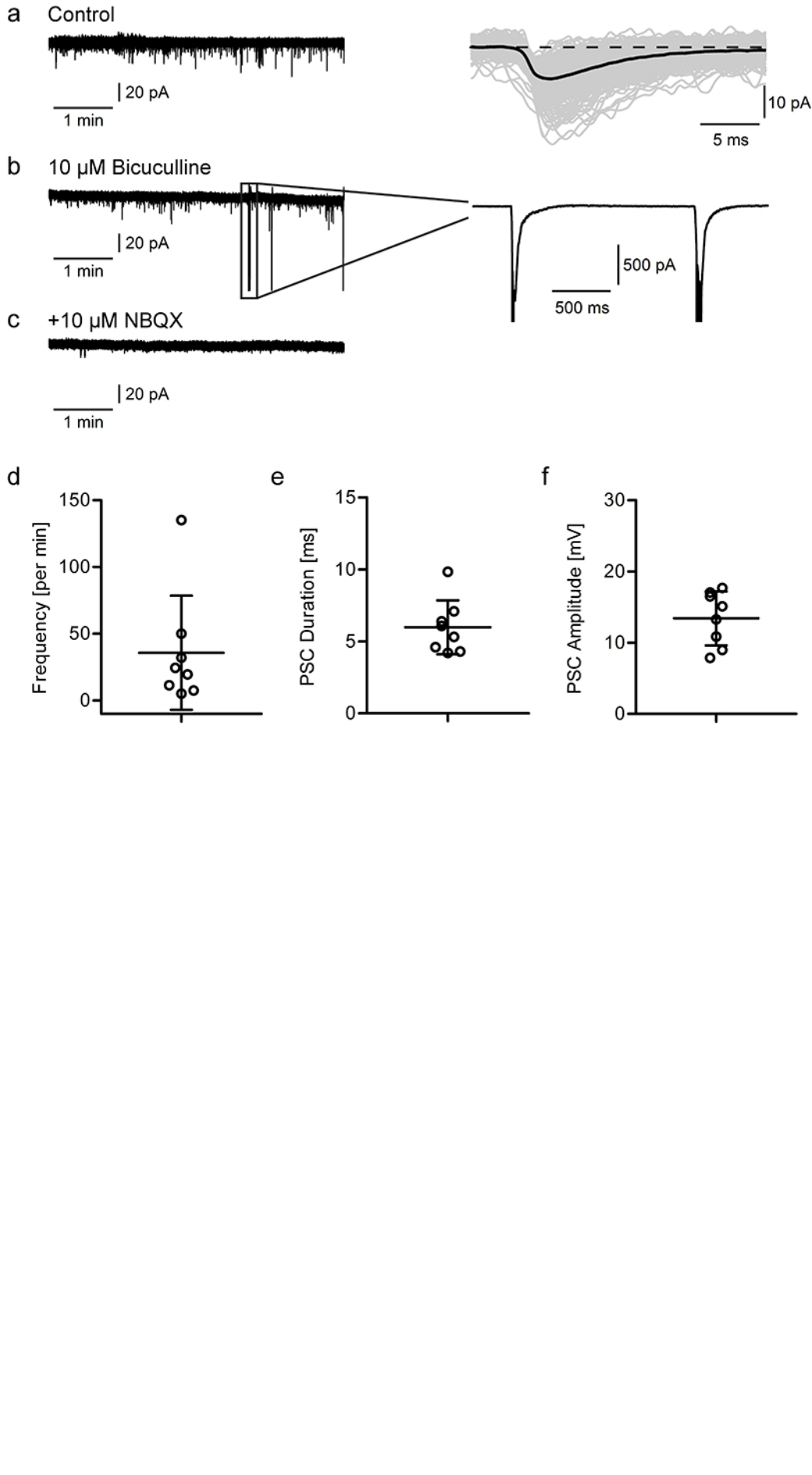
a
Control
20 pA
1 min
10 pA
5 ms
b
10 μM Bicuculline
20 pA
1 min
500 pA
500 ms
c
+10 μM NBQX
20 pA
1 min
d
Frequency [per min]
150
100
50
0
e
PSC Duration [ms]
15
10
5
0
f
PSC Amplitude [mV]
30
20
10
0

Table 1

	GFP^{pos}	GFP^{neg}	GIN	PC
Soma diamater [µm]	40.2 ± 2.5	41.9 ± 6.3	46.0 ± 6.7	47.6 ± 6.2
		ns		
Number of primary processes	4.4 ± 0.97	5.25 ± 0.5	5.4 ± 1.34	5.8 ± 1.3
		ns		
Total dendritic length [µm]	2926 ± 381	2642 ± 975	1711 ± 490	4266 ± 1330
		PC vs GIN***, GFP^{pos} vs PC*, GFP^{neg} vs PC*		
Total number of dendrite branching points	22.6 ± 4.2	17 ± 8.5	16.8 ± 3.6	37.8 ± 7.9
		PC vs GIN***, GFP^{pos} vs PC***, GFP^{neg} vs PC***		
Maximal dendritic complexity	10.4 ± 2.3	7.25 ± 1.5	6.2 ± 1.3	13.6 ± 5
			GIN vs PC**, GFP^{pos} vs GIN*	
Total dendritic area [µm^2]	6189 ± 716	5241 ± 2324	2472 ± 675	7595 ± 3241
			GIN vs PC**, GFP^{pos} vs GIN**	
Total axon length [µm]	2153 ± 965		6597 ± 2594	
			GFP^{pos} vs GIN**	